

## Earth-Based Visible and Near-IR Imaging of Mercury

Leonid Ksanfomality · John Harmon · Elena Petrova ·  
Nicolas Thomas · Igor Veselovsky · Johan Warell

Received: 20 March 2007 / Accepted: 25 October 2007 / Published online: 12 December 2007  
© Springer Science+Business Media B.V. 2007

**Abstract** New planned orbiter missions to Mercury have prompted renewed efforts to investigate the surface of Mercury via ground-based remote sensing. While the highest resolution instrumentation optical telescopes (e.g., HST) cannot be used at angular distances close to the Sun, advanced ground-based astronomical techniques and modern analytical and software can be used to obtain the resolved images of the poorly known or unknown part of Mercury. Our observations of the planet presented here were carried out in many observatories at morning and evening elongation of the planet. Stacking the acquired images of the hemisphere of Mercury, which was not observed by the Mariner 10 mission (1974–1975), is presented. Huge features found there change radically the existing hypothesis that the “continental” character of a surface may be attributed to the whole planet. We present the observational method, the data analysis approach, the resulting images and obtained properties of the Mercury’s surface.

---

L. Ksanfomality (✉) · E. Petrova · I. Veselovsky  
Physics of Planets, Space Research Institute, 84/32 Profsoyuznaya str., Moscow 117997, Russia  
e-mail: ksanf@iki.rssi.ru

E. Petrova  
e-mail: epetrova@iki.rssi.ru

I. Veselovsky  
e-mail: veselov@decl.sinp.msu.ru

J. Harmon  
National Astronomy and Ionosphere Center, Arecibo Observatory, Arecibo, PR 00612, USA  
e-mail: harmon@inaic.edu

N. Thomas  
Physikalisches Institut, University of Bern, Silderstr, 5, 3012 Bern Switzerland  
e-mail: nicolas.thomas@phim.unibe.ch

J. Warell  
Astronomika Observatoriet, Uppsala Universitet, 751 20 Uppsala, Sweden  
e-mail: Johan.Warell@astro.uu.se

**Keywords** Solar system · Unknown side of Mercury · Ground based observation · Resolved images · Regolith physical properties

## 1 Challenges of Ground-Based Observations of Mercury

Because of the small angular diameter of Mercury, about 7 arcsec in a favourable configuration, and its small angular distance from the Sun (on average not exceeding  $22^\circ$ ), the task of obtaining distinct images of its surface from Earth-based observations is extremely difficult. Few astronomers drew maps of Mercury (e.g., Antoniadi's map of Mercury, 1934). In the middle of the 20th century, several attempts were made by French astronomers (Dollfus 1961). Figure 1 shows several drawings made from visual observations of the planet by B. Lyot in 1942 (Fig. 1a) and A. Dollfus in 1950 (Fig. 1c). Due to the orbital resonance of Mercury relative to Earth, at both inferior and superior conjunctions practically the same sides of the planet are observed in turn. At the time of their observations, Lyot and Dollfus did not know about the 3 : 2 resonance of Mercury; they assumed that the planet rotates synchronously (Dollfus 1961). Only those experts who have observed themselves by telescope the scarcely resolvable disk of Mercury can estimate the achievement of Lyot and Dollfus whose drawings are so similar and, as shown in the following, reflect a reality of the largest formations on Mercury, as shown in Figs. 1a and 1c. Both drawings (Fig. 1a,c) coincide exactly with the position of the planet shown in Fig. 1b, for which nowadays the mosaic of Mariner 10 photos is available. [Here and in the following the electronic globe generated by the RedShift 4 code is used (Red Shift 4 2000)]. In 1974–1975, three flybys of Mercury were made by Mariner 10. Imaging of the planet by Mariner 10 covered only 46% of the planet's surface (Fig. 2), so that after the Mariner 10 mission the other, unobserved side of the planet became the main object of interest.

Observing Mercury by classic astronomical methods is difficult due to well-known handicaps caused by the terrestrial atmosphere. These handicaps impede observation of very small objects close to the horizon. One can imagine the atmosphere's heterogeneity as a random set of poorly refracting lenses, each of them in its own way deforming the image. The distortions are individually insignificant, but they accumulate. Other kinds of difficulties are the jitter of images and their washout, caused by the atmosphere's turbulence. An obvious method of improving astronomical images (besides adaptive optics techniques) is the reduction of their exposure to a duration during which turbulence does not spoil a picture. If one then selects from the large number of pictures with very short exposures those which have small distortions, their processing makes it possible to approach the diffraction limit of the instrument. Experiments of this sort were carried out in 1960s–1970s, but without a noticeable success. The exposure should be very short, on the order of milliseconds for a telescope

**Fig. 1** Drawings of Mercury made by B. Lyot in 1942 (a) and A. Dollfus in 1950 (c) at visual observation of the planet. The view of the planet in this phase, constructed from a mosaic of photos made by Mariner 10 is placed in the centre (b). The central meridian is  $110^\circ$ W

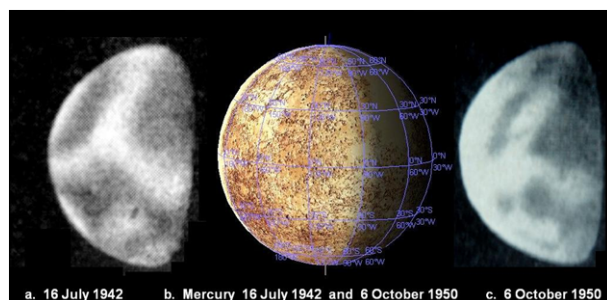


**Fig. 2** In areas it investigated, the Mariner 10 found cratered terrains (yellow), volcanic plains (blue) and crater units on Mercury (Head III 1981). White = unknown areas

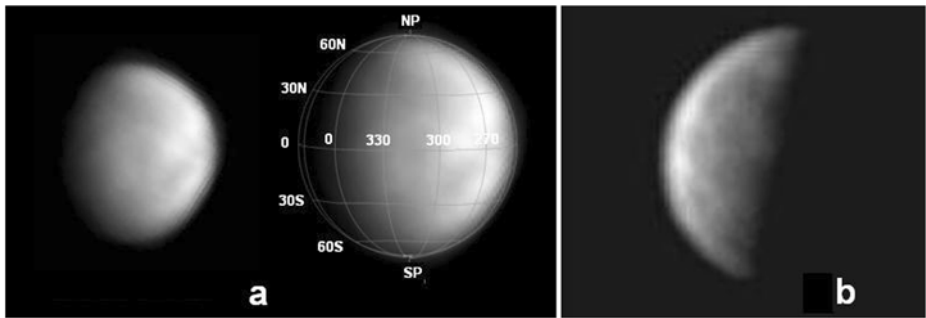
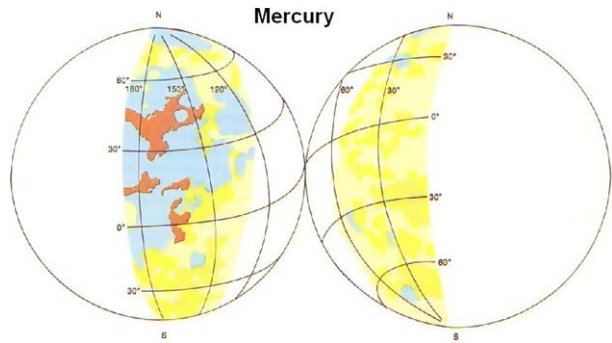
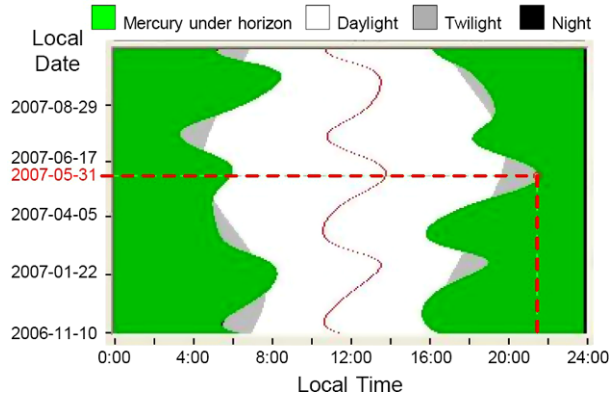


**Fig. 3** The modern amateur's stacked photos of Mercury acquired by means of a small telescope and CCD matrix. **(a)** Image of Mercury obtained with a 10-inch telescope, October 1, 2006. Camera exposures were 1/50 s, a spectral range 700–900 nm, peaking at 800 nm. The image is a stack of 70 of the best single frames. North is up. Courtesy of S. Massey, Australia. **(b)** The image obtained with another 10-inch telescope using a red filter. The 100 images, each of 1/73 s, were stacked. Observation made during the daytime, November 22, 2006, with Central Meridian of 271°W. Courtesy of A. Allen, Santa Barbara, California

of moderate size (1.2–2 m); this is orders of magnitude shorter than the exposure needed by photographic emulsions. Nevertheless, a map of the planet was produced photographically (Murray et al. 1972). The millisecond exposures needed became possible when new, highly effective CCD detectors could be used in combination with computer programs that could process large volumes of observational data. The availability of CCDs nowadays allows us to obtain photographs of Mercury using even small telescopes, 20 to 36 cm. Several amateur astronomers are now obtaining excellent images of Mercury (Fig. 3).

The brightness of the sky is another problem. Observations of Mercury are inevitably made in twilight or even in daytime, against a bright sky. Brightness of the clean sky (produced by Rayleigh scattering) sharply decreases as the wavelength  $\lambda$  increases, as  $\lambda^{-4}$ . Shifting the centre of the spectral range, say, from 600 nm to 800 nm, decreases the sky brightness more than three times. The investigation of the surface of the atmosphereless celestial body yields usually the same results, whether they are grey or in colour (however, the colour hues may be of importance for mineralogy). That is why using near IR is very useful if the CCD spectral response is high enough in the IR range (see the discussion and Fig. 11). For the same reason, only observations at high mountain observatories are usable. Using the IR range is of importance in other ways, too. During twilight observations, Mercury is low above the horizon; this is the reason for a strong differential refraction and especially differential chromatic refraction. Selection of the IR range partly solves this problem. Due to

**Fig. 4** Twilights observability of Mercury is limited by two or three short favorable periods each year. The diagram shows morning (*left*) and evening (*right*) elongations for one year, starting November 10, 2006. The deeper the grey area, the better conditions are



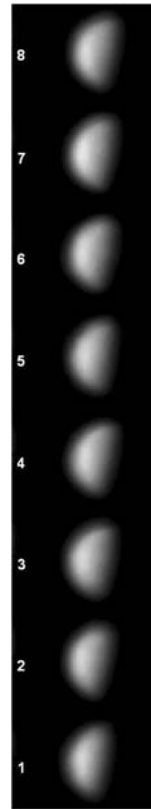
the reasons mentioned in this paper, the spatial resolution of astronomical images depends on the place of observation, time of day, density of aerosol component, zenith distance of Mercury (air mass, or  $\sec z$ ) and, primarily, on length of exposure.

As the angular distance of Mercury from the Sun in ground-based observations is always small, observatory administrators are reluctant to use large telescopes to observe Mercury, since there is a risk that the instrumentation of the telescope could be damaged by direct solar rays. Nevertheless, ground-based observations of Mercury by “classical” methods (without using short exposures) have been performed by many researchers. A detailed list of such observations can be found in the review by Warell and Limaye (2001). In comparison with the observations of other bodies in the Solar System, observations of Mercury at ground-based observatories are also subject to many restrictions. Since the greatest elongation of the planet does not exceed  $28^\circ$  (typically, no more than  $22^\circ$ ), observations must be performed within less than 1 hour; in fact, the observing time in twilight rarely exceeds 20–30 min, as the planet is very low above the horizon when the large air mass ( $\sec z$ ) complicates the problem still further. More or less usable observations of Mercury are possible only at low-latitude mountain observatories. However, as is shown in the following, resolved images of the planet can still be obtained by ground-based technical and analytical means, although at the very limit of technical capabilities. There are three to four Mercury morning and evening elongations each year at which observations are feasible in principle. Figure 4 is calculated for Arhiz, the site of the Special Astrophysical Observatory in the Caucasus. Due to the inclination of planet’s orbit to the ecliptic, not more than two of each set of elongations are really favourable with respect to the duration of visibility, indicated in gray in Fig. 4. As an example, the dashed lines indicate that on May 31, 2007, the year’s most favourable elongation, Mercury sets on the mathematical horizon at 21:28, when sunset is 19:38. Keeping in mind that the planet is observable at least at few degrees above horizon, the duration of evening session for these favourable 10–12 days will each be less than one hour.

## 2 Advantages of a Short-Exposure Method and Achievable Surface Resolution

The characteristic time for which instant optical properties of atmosphere could change may be determined by researching frequency spectra of stellar scintillation and image jittering. It is seldom shorter than 30 ms (Ksanfomality 2003). Therefore, to use instant calm atmosphere, the exposure time should not be longer than that time. Advantages of the method

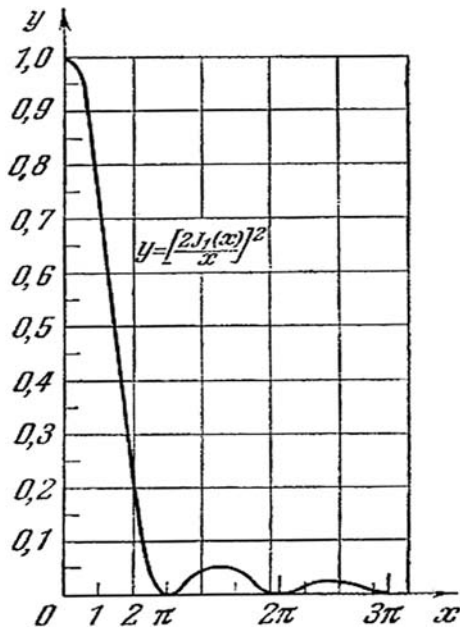
**Fig. 5** Fast changes of quality in images of Mercury. Time increases with images numbered from down to up. Only images 2, 6 and 8 are precise (more or less). Image 1 is blurred; 3 is deformed. Image 4 is blurred along  $X$  axis and rotated; 5 is blurred along  $Y$  axis; 7 is deformed and appreciably differ from the distinct image 2. Intervals between photos are 99 ms. Expositions are 3 ms



of short exposures were considered by Fried (1978), following Hufnagel (1966). In Fried's words: "In short-exposure imaging through turbulence, there is some probability that the image will be nearly diffraction limited because the instantaneous wave-front distortion on the aperture was negligible". Fried analyzed distortions created by atmospheric inhomogeneities and estimated that the possible gain in the resolution can be a factor 3.4 at short expositions. One of his conclusions was that optimum observations are before dawn, when atmospheric turbulence has not yet begun; for daytime observations (with moderate zenith distances) the relatively long exposures need the presence of strong winds. Experimental backing for these conclusions are available in both cases. We can attest to the correctness of these statements because three of the most successful series of our observations of Mercury were made in such conditions—two different sets were made during early autumn mornings in two different observatories, and another during spring evenings when observations at the Skinakas observatory were carried out in conditions of very strong winds. These results can be counted as a strong backing of Fried's (1978) conclusions. However, another of his conclusions, that "the probability of getting a good image" sharply decreases when diameter of telescope  $D$  grows, seems to be debatable, as he did not take into account, apparently, that exposure with a 1.5-m telescope can be about 10 times shorter than with a 0.5-m telescope, at the same signal-to-noise ratio.

In Fig. 5, part of a sequence of electronic pictures of Mercury (from observations made May 2, 2002) with an exposure of 1 ms, separated by intervals of 99 ms, shows how fast the quality of an image may change. Time increases with images from bottom to the top. Only

**Fig. 6** Distribution of intensity in the image point. Three bright and dark rings are shown



images 2, 6 and 8 are precise, more or less. Other images are deformed and appreciably differ from the distinct image 2.

Steadier weakening or strengthening of atmospheric instabilities appear and disappear within several seconds (or tens of seconds). Another problem (besides blurring) is that in a series of a large number of electronic pictures, images sometimes appear rotated by a few degrees (Ksanfomality 2003) and that complicates their joint processing.

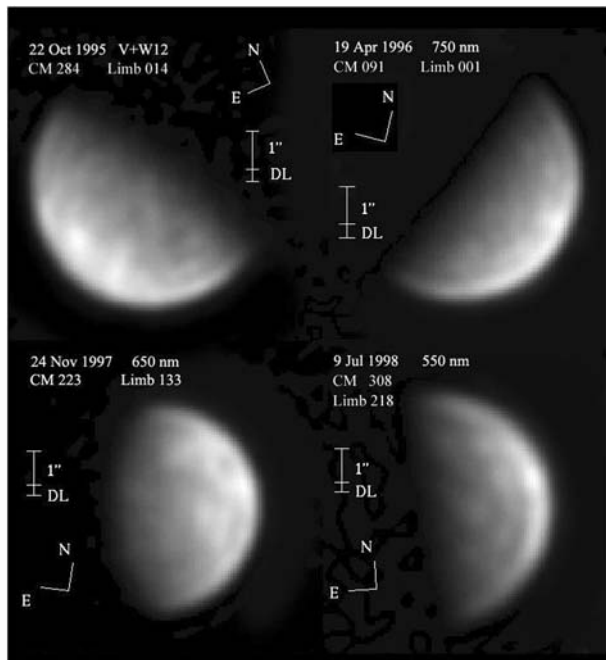
Returning to the potentially achievable resolutions and comparing them with the diffraction limit of an instrument, it is necessary to keep in mind that stacking very large numbers of primary pictures improves images substantially. As shown in the following, it is possible through this method to resolve details which are in size formally below a diffraction limit of the telescope. For the case of observations of Mercury in 90° phase (at geocentric distance 0.85–0.90 AU), in a near-IR range, as mentioned earlier, using the instrument with diameter, say,  $D = 1.25$  m, at a wavelength  $\lambda = 600$  nanometer, the formal diffraction limit is  $1.22 \lambda/D = 0.15$  arcsec. Thus, limiting resolution on the surface of the planet corresponds exactly to 100 km. Therefore the details of surface features of sizes of 40–80 km, considered below, should apparently be outside the capabilities of this method. However, this is only seemingly a paradox. As is known, distribution of intensity  $y$  on distance  $x$  from the centre of the image makes  $y = [2J_1(x)/x]^2$ , where  $J_1$  is the coefficient of the first term in the polynomial expansion describing the ring pattern, and the factor  $1.22\pi$  corresponds to position of the first minimum. If one chooses details at a level higher than 0.5 or 0.7 (Fig. 6), for example, at 0.9 level, their size, naturally, will be less. But it needs a very large number of suitable raw pictures (as is carried out in our program of stacking of images). Obtaining a resolution close to the diffraction limit of the instrument should make a resolution of, say, 0.12–0.15 arc seconds, using sharp optics, of course. At the same time, typical resolution for a 1.5-meter 1/10 reflector is seldom better than 1–1.3 arc seconds, being limited by atmospheric turbulence. Thus, it was impossible to obtain images resolved at the diffraction limit for Mercury, with a diameter in a quadrature phase on average is only

7.3 arc seconds, using photographic materials that do not allow reduction of exposure time to units of milliseconds. Such an image could be resolved typically to four to six lines only, as the photographic resolution is about 1.3 arc sec. Only with the advent of CCD detectors that have high quantum output, combined with fast image processing techniques that permit the combination of thousands of images chosen for high quality, does the high spatial resolution become achievable. It should be mentioned that a long-focus instrument has advantages in observing Mercury because that increases nominal resolution, which is important for the subsequent data processing.

### 3 Pioneering Short-Exposure Imaging of Mercury

Pioneering multicolour filter imaging of Mercury with rather short exposure times was made by J. Warell at the astronomical observatory Uppsala, Sweden (Warell and Limaye 2001). Warell began observations in 1995 at the 0.5-m Swedish Vacuum Solar Telescope (focus 22.35 m), on La Palma in the Canary Islands, at 11 wavelengths from 429 to 944 nm, using fast-readout CCDs. Two CCD cameras with 1.4 and 1.6 Mpixels were used with exposure times from 25 up to 360 ms. The outcome of a multiyear effort to map albedo variations of the global surface of Mercury at optical wavelengths was presented by Warell and Limaye (2001). They showed single (not stacked) pictures chosen from their large data set, using images of different parts of Mercury obtained during the elongations 1995–1998. Examples of successive electronic photographs of Mercury taken by J. Warell at the La Palma Observatory in the period 1995–1998 are shown in Fig. 7. Based on these sets, the images were produced that are shown in Fig. 8, (a) globes and (b) rectilinear map. The authors stated that a resolution  $\sim 200$  km was realized. Despite the rather long exposure time for the single images, large details are defined and have permitted the authors a wealth of geologic

**Fig. 7** Examples of electronic photographs of Mercury taken by J. Warell in period 1995–1998. Single Mercury images obtained with the 50 cm Swedish Vacuum Solar Telescope on La Palma observatory on four dates, from 1995–1998. The central meridian and limb West longitudes are indicated. Scale bars for 1 arc second and the diffraction limit are given for the used wavelength (Warell and Limaye 2001)



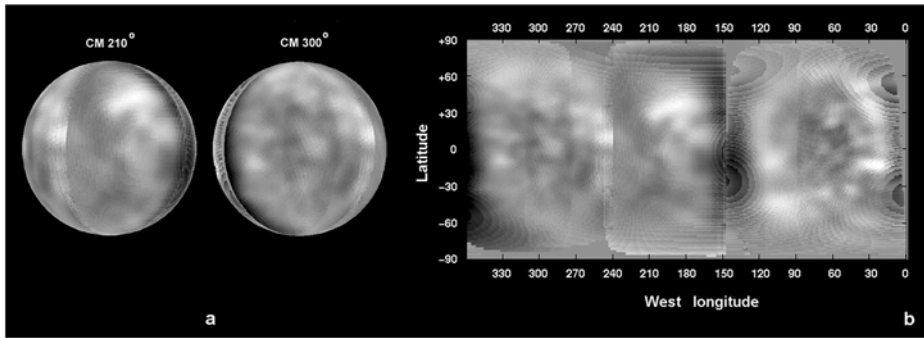


**Fig. 8** (a) Globes and (b) global cylindrical projection of Mercury images created by J. Warell from the same ground-based observations as in Fig. 7. The central meridian is indicated as CM (Warell and Limaye 2001)

interpretations (see Sect. 10) based on multicolour analysis (Warell 2002, 2003; Warell and Valegård 2006).

Figures 8a,b are the first global map of Mercury's surface produced using CCD imaging. For this, the selected high-resolution raw images were individually reduced according to standard CCD procedures, sharpened by Wiener filtering to increase definition and contrast, and photometrically rectified and remapped for detailed analysis. The studies that were made of the morphologic and photometric properties of the detected albedo features, and their correlation with Mariner 10 image data of the well-known hemisphere, allowed identifications of probable bright ray craters on the poorly known hemisphere. Warell and Limaye (2001), as well as Warell and Valegård (2006), noted that in many ways the two hemispheres were found to be remarkably similar; no statistically significant differences could be detected in a comparison of the spatial distributions, number densities, photomorphologic variables or colour properties for the features on the two hemispheres. From a study of the Mariner 10 image data it was concluded that about 70% of the bright features on the poorly known hemisphere could be attributed to bright ray craters, while the rest were attributed to bright crater floors, concentrations of crater rays or diffuse patches which had been described based on Mariner 10 images. One feature corresponding to the location of the ray crater Kuiper ( $11.3^{\circ}\text{S}$ ,  $31.1^{\circ}\text{W}$ ) discovered by Mariner 10, was found to be extraordinary in all its morphological parameters, with a contrast relative to the darkest albedo features of as much as 50%. Localized dark patches were found to correlate with surface of low radar backscatter signal (Harmon and Slade 1992; Slade et al. 1992; Butler et al. 1993). Bright spots were found to be less well correlated with radar signatures, but a bright albedo feature at  $331^{\circ}\text{W}$ ,  $3^{\circ}\text{N}$ . The spots A and B detected in radar works were found to coincide with locations of less bright and more extended albedo features.

About this time papers were published (Ksanfomality, 2004, 2003) describing a new approach to the processing of Mercury's images. Subsequently, to produce a more detailed image of the planet, Warell passed the primary photographs to L. Ksanfomality to be processed by the software package (Ksanfomality, 2004, 2003; Ksanfomality et al. 2005). Unfortunately, because of the limited number of primary photographs, the software failed to perform a satisfactory correlation in matching the planetary images.

Another important pioneering work on short-exposure imaging of Mercury, simultaneously with Warell and Limaye (2001), was carried out by Dantowitz et al. (2000) and Baumgardner et al. (2000). On August 29, 1998, they electronically photographed Mercury in the

**Fig. 9** Mercury image from 275° to 330°W longitude was produced by a short exposure technique and subsequent processing of a large number of data files by: (a) Dantowitz et al. (2000), (b) Baumgardner et al. (2000). A stack and co-add of (a) and (b) using the method of Ksanfomality (2004, 2003) is shown in (c). From Ksanfomality (2006)

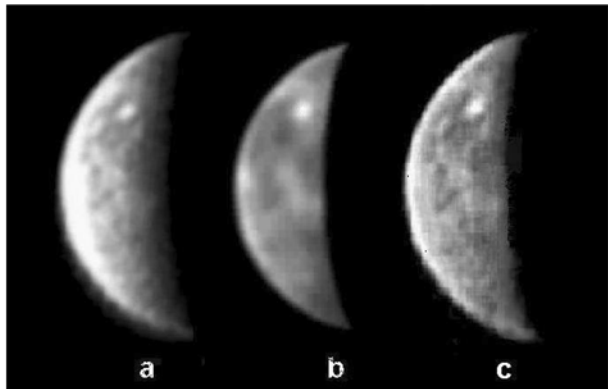
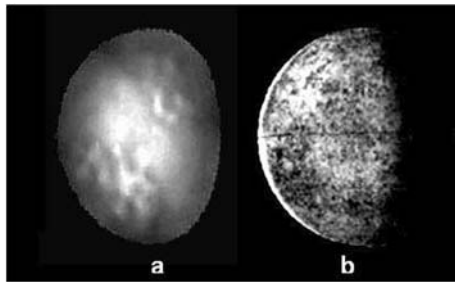


**Fig. 10** Stacked image of Mercury from the observations at AbAO on December 3, 1999

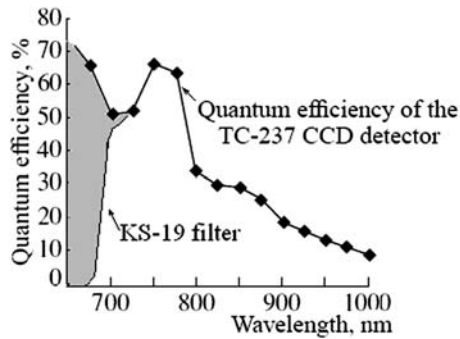


longitude range that was not imaged by Mariner 10 (in 1974–1975), using an ordinary (general purpose) video camera mounted on the 1.5-m Mount Wilson Observatory telescope. The video camera was operated in standard mode, with a frame rate of  $30 \text{ s}^{-1}$  and an exposure of 17 ms. A total of 219,000 frames were taken, of which 1,000 photographs were chosen for further processing. Eventually two sets of 30 images with the highest contrast scores were used to portray the final results. Mercury was imaged at phase  $106^\circ$ , in the longitude range  $265\text{--}330^\circ\text{W}$ , and with the coordinates of the subterrestrial point  $7.7^\circ\text{N}$ ,  $254^\circ\text{W}$  (Figs. 9a,b). This, we believe, was the first published result of stacking this large number of unprocessed electronic photos of Mercury; the author's stacked images were probably the best results of the works published in 2001–2002. Dantowitz et al. (2000) and Baumgardner et al. (2000) estimated the achieved resolution on the surface of Mercury to be 250 km. A review of all these results was published by Mendillo et al. (2001).

The results by Dantowitz et al. (2000) and Baumgardner et al. (2000) were processed additionally by the method presented in papers by Ksanfomality (2002, 2004) and Ksanfomality et al. (2005), for the reason given in Sect. 5. The processing improved appreciably the image of the planet (Fig. 9c) and permitted distinct large details to be defined. The stacked image Fig. 9c appears more detailed than the original images.

In December 1999, Ksanfomality et al. (2001) took a series of raw electronic photographs of Mercury at the Abastumany Astrophysical Observatory (AbAO) of the Republic of Georgia ( $42^\circ 50'\text{E}$ ,  $41^\circ 45'\text{N}$ ), using a ST-6 CCD camera mounted at the Cassegrain focus of the AZT-11 telescope ( $D = 1.25 \text{ m}$ ,  $F = 16 \text{ m}$ ). Using these images, they performed tests of different kinds of processing by stacking software and produced a trial image in which some features could be distinguished (Fig. 10). The longitudes in the image were close to

**Fig. 11** The spectral range of the CCD camera and filter that were used for all images shown in the following



the electronic globe created from the published mosaics of Mariner 10, which allowed their comparison.

On November 3, 2001, the next series of observations of Mercury were performed at the ABAO again during morning elongation of the planet. The phase of the planet was  $63^\circ$ . The same AZT-11 telescope was used, but with a 700-nm filter that cut off the short wavelengths and with the STV CCD camera produced by SBIG Co (pixels are square  $7.4 \times 7.4 \mu\text{m}$ ). The long-wavelength boundary was near  $1 \mu\text{m}$  (Fig. 11) and was determined by the spectral properties of the CCD array. (It should be mentioned that the same camera and filter were used for all images shown in the following.) Since the object is bright, the integration time of several thousand signal units in each pixel even with a small-pixel CCD array still did not exceed a few milliseconds and short exposures, 3–10 ms, were used. On November 3, 2001, the disk of the planet was seen at an angle of 6.1 arcsec, which corresponded to a linear image size of 0.43 mm in the focal plane of the telescope. The observations were carried out under extremely favourable visibility conditions (Ksanfomality 2002). Several series of raw photos, including a series with the recording of the light polarization distribution over the planetary disk, were taken (Ksanfomality 2002). Based on the subsequent selection from the electronic raw photos, an image for the longitudes from  $90^\circ$  to  $190^\circ$  was produced (Fig. 12), using the first version of the data processing by means of correlational stacking software. In this experiment, when initial photos were stacked, a high resolution was achieved at the central part of the image that looked sharp. However, the image's periphery was blurred. The image of Mercury thus obtained was compared again with the electronic mosaic globe made from Mariner 10 photos, for the same phase and longitudes. This showed that features in the central part of the image with sizes of only 100–250 km are clearly identified with Mariner 10 data (Fig. 12). Later other features were also identified. At that time, this result was unexpected since the feature sizes were at the diffraction limit of the telescope, but it convincingly proved the actual capabilities of the new method. An example of coincident features in two image fragments is illustrated in Fig. 13, where 13a and 13c are fragments of Fig. 12; Figs. 13b and 13d are fragments of the Mariner 10 mosaic map, with coincident features indicated by arrows in b and c. A small, very dark area ( $22^\circ\text{N}$ ,  $155^\circ\text{W}$ ) is marked as 1. Large features at ( $15^\circ\text{S}$ ,  $150^\circ\text{W}$ ) and ( $18^\circ\text{S}$ ,  $165^\circ\text{W}$ ) are indicated as 2 and 3. A minor bright dot 4 ( $10^\circ\text{S}$ ,  $117^\circ\text{W}$ ) in Fig. 12a and Fig. 13c coincides with an unnamed bright crater 4 in Tolstoy, or Phaethontias Region (Fig. 13b). Two large, dark rounded regions 5 and 6 near the equator (centred on  $5^\circ\text{N}$ ,  $124^\circ\text{W}$  and  $1^\circ\text{S}$ ,  $135^\circ\text{W}$ ) have the same form in Fig. 13b and c. These regions include the craters Mena ( $0.5^\circ\text{N}$ ,  $125^\circ\text{W}$ ) and Lysippus ( $1.5^\circ\text{N}$ ,  $133^\circ\text{W}$ ). Most convincing is a coincidence of shapes of features 4, 5, 6 in the 13 b and c images.

The features in other areas were also identified. Some details in Fig. 12a may be due to noise in view of the limited number of original images. Nevertheless, the similarity of the

**Fig. 12** (a) Image of Mercury stacked from initial photos of observations made on November 3, 2001, and (b) its comparison with the globe of Mercury constructed from the Mariner 10 photo mosaic (from Ksanfomality and Sprague 2007, reworked)

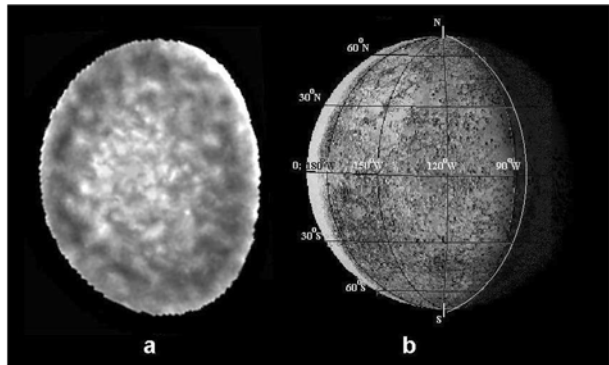


**Fig. 13** Comparison of the fragments of the stacked image (a, c) and the Mariner 10 mosaic photomap (b, d)

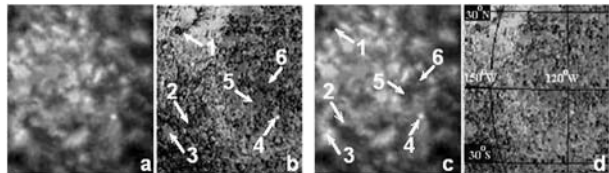
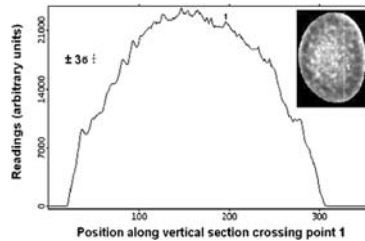


**Fig. 14** Data counts from a trace across the image of Fig. 12a along the vertical line parallel to the polar axis and crossing the bright point (marked 4 in Fig. 13). From Ksanfomality and Sprague (2007)



two images in Fig. 13 is obvious, despite the small size of the formations presented here (feature 3 is only 200 km in width). After all processing, the contrast of elements of features in the stacked image of Mercury in Fig. 12a is within the range 4–10%.

Figure 14 shows the distribution of contrast features in the section parallel to the polar axis and passing through the bright dot ( $10^{\circ}\text{S}$ ,  $117^{\circ}\text{W}$ ) in Figs. 12 and 13. The position of features across the section is marked on the linear scale. Ksanfomality and Sprague (2007) estimated that the root mean square (rms) error for a signal obtained from one (single) pixel of the CCD for the case of Fig. 12 is about 9% for the absolute rms errors and 0.7% for the relative rms errors. The triple error  $3\sigma R \approx 2\%$ , that was quite comparable to the contrast of individual pixels (4–10%), as in Fig. 14. However, since the image is formed not by a single pixel, but by a large group of pixels (1,200 pixels in Fig. 13a), the probability of their erroneous combination is much lower.

Thus the first steps of the data processing by the correlational stacking software proved its efficiency. The data processing program was not perfect. Large image features were suppressed; the contrast of light and dark features was quite low; and the periphery of the image was blurred.

During subsequent years more effective codes were worked out, as described in the next section. In particular, the application of these codes successfully showed both the low spatial frequencies and a distinct periphery of the image.

#### 4 Imaging Surface of Mercury in 2003 (Longitudes 90–190°W)

During the next few years, different data-processing programs were tested. Eventually it was found that less complicated codes yielded better results. The code AstroStack, created by Stekelenburg (1999, 2000), and the AIMAP code, created by Kakhiani (2003), were chosen to form the core of the processing system (Ksanfomality 2002). The technique of processing and confirmation of the results included about 10 other codes. The most important procedure was the correlation stacking of a large number of images. A short description of the processing technique was presented by Ksanfomality (2002) and Ksanfomality et al. (2005). Its newer version showed successfully both large image features and a distinct periphery of the image.

Together with the processing technique, a new, more effective method of observation was developed. To take the largest possible number of primary electronic photographs of Mercury, the STV camera mounted on the telescope was switched to fast image collection mode. It took 4 s (at a 1-ms exposure with 99-ms intervals) to acquire one frame (Fig. 15) composed of 40 photographs. It took approximately the same time to write the frame to a memory. After 15 frames were obtained, the entire set was transferred to a computer.

The STV camera is not the best solution. Only a serial (com) port is used in the STV camera for data transfer, which causes additional delays and is a shortcoming of the STV camera. Nevertheless, the fast collection of primary images of each frame in some measure compensates for these disadvantages. However, this requires stable seeing conditions, which are rarely met. The observational data acquired with the STV camera in its chosen mode had an 11- or 11.5-bit compressed format. The routine primary data processing operations included a precheck (the rejection of defective series), by which the best series of undistorted electronic photographs or single images were selected. For the case when visibility is poor even a single good image should be selected for processing.

A new series of observations of Mercury were made on November 2, 2003, under the same circumstances that were described about the observations made on November 3, 2001. The stacked and additionally processed image (Fig. 16) covers an area investigated by Mariner 10. The position of the planet was essentially the same as in Fig. 12 (64° is the phase of the planet, 120° is the central meridian). The longitudes 90–190°W are known after the Mariner 10 mission; however, the view of the planet in Fig. 16 differs much from the Mariner 10 images (e.g., Fig. 12b), by an abundance of dark and light areas. The stacked image in Fig. 16 much more closely resembles the far side of the Moon than the widely known and often published mosaic of Mariner 10 photographs. The main reason is that the Mariner 10 mosaic was created manually (Strom and Sprague 2003); the contrast of small features in the primary photographs was enhanced, and the boundaries of the photograph fields required alignment and were matched in contrast. This led to the suppression of the

**Fig. 15** Example of a frame from a group of primary electronic photographs of Mercury (November 24, 2006). The exposures are 3 ms each, the intervals are 99 ms; the size of each photograph is about 7 arcsec

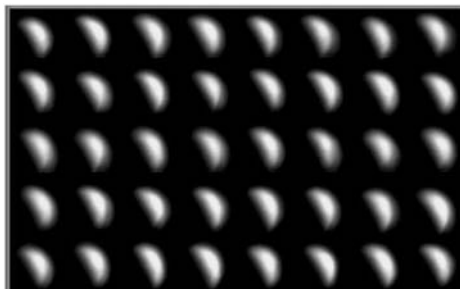
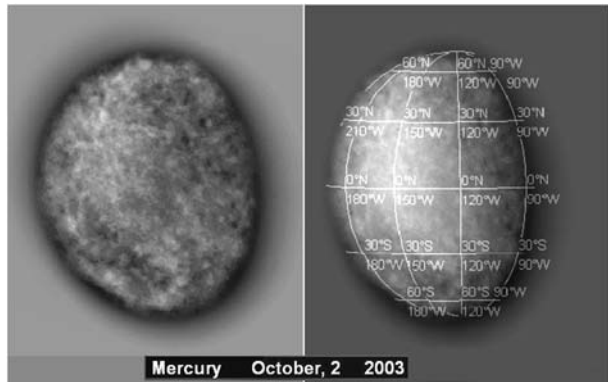


**Fig. 16** (a) Image of Mercury stacked from initial electronic photos of observations made on October 2, 2003, and (b) coordinate grid of Mercury for this date



low spatial frequencies, corresponding to the large structures lost in the Mariner 10 mosaic. However, it may well be that there is another reason. The onboard system memory is known to have malfunctioned during the operation of the spacecraft near Mercury. It is possible that this led to a mismatch of the video channel frequency properties of the Mariner 10 camera. In any case, the balance of spatial frequencies of the mosaic images was disrupted, due at least in part to the manual processing.

Though the resolution in Fig. 16 is not as high as in the central part of Fig. 12a, large details are seen better. The accuracy of the coordinate grid position is within  $5^\circ$ . In the left part of Fig. 16 the limb is placed a bit to the west, compared to the borders of imaging by Mariner 10 (Fig. 12b). In the Northern hemisphere, northward from the Mozart crater ( $8^\circ\text{N}$ ,  $190^\circ\text{W}$ ) and westward from Caloris Planitia ( $30^\circ\text{N}$ , westward from  $180^\circ\text{W}$ ) a blurred large area is placed along the limb. This is the area of quadrangles Tolstoj H-8, Shakespeare H-3 and H-4 (Liguria), according to the *Atlas of Mercury* (Davies et al. 1978). A large, dark basin is placed at  $45\text{--}60^\circ\text{N}$ , westward from  $180^\circ\text{W}$  on the limb ( $10^\circ$  on Mercury's equator corresponds to 426 km). Close to the North Pole there are two dark round basins, 300–500 km each. A very large dark area, extending for 1,300 km along the meridian, has an irregular shape. It coincides partly with the Basin Shakespeare. A bright crater at  $40^\circ\text{N}$ ,  $120^\circ\text{W}$  could be its centre. Two distinct round craters are placed in its southern part  $20^\circ\text{N}$ ,  $115^\circ\text{W}$  and  $30^\circ\text{N}$ ,  $110^\circ\text{W}$ . Southward from them, a dark elongated feature about 400 km is centred at  $20^\circ\text{N}$ ,  $90^\circ\text{W}$ . It is remarkable that many prominent dark or bright features, although they are well outlined (like a dark basin at the centre of the image), do not coincide with any known objects. The Basins Shakespeare, Van Eyck and Strindberg are difficult to identify. In the Southern hemisphere, two large dark basins are seen at  $50^\circ\text{S}$ ,  $110^\circ\text{W}$  and  $50^\circ\text{S}$ ,  $150^\circ\text{W}$ , about 400–500 km. An elongated bright area centred at  $25^\circ\text{S}$ ,  $170^\circ\text{W}$ , is adjusted to a dark elongated valley, centred at the limb at  $25^\circ\text{S}$ ,  $190\text{--}200^\circ\text{W}$ . The smallest features about 200 km (appearing as dark dots) are seen at  $20^\circ\text{S}$ ,  $170^\circ\text{W}$ . A chain of dots about 200 km each is seen from  $30^\circ\text{S}$ ,  $140^\circ\text{W}$  to  $55^\circ\text{S}$ ,  $130^\circ\text{W}$ . For more reliable imaging one needs many more primary electronic photos.

As for initial photographs of Mariner 10, they are rich in bright and dark features (Fig. 17a). Here Caloris Planitia and the Mozart crater (marked CP and M) are seen at the morning terminator. The photo was made 12 hours after closest approach of Mariner 10. The image consists of two parts; they are joined at a line that crosses the Tolstoj basin (marked by T in Fig. 17a). Their boundary (just above mark "T") is well seen at the limb. Despite a minor phase difference, the upper photo shows the basin to be dark, the lower bright. This phenomenon is considered in Sect. 8; the 17b panel is considered in Sect. 7.

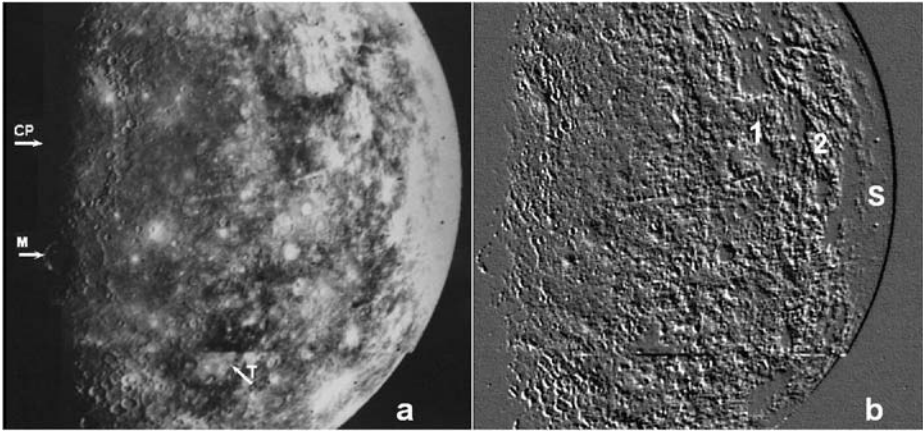


**Fig. 17** (a) Unprocessed images of the Mariner 10 are rich in bright and dark areas. *CP* = Caloris Planitia, *M* = Mozart crater, *T* = Tolstoj basin. (b) Using high-pass filter provides quasi-relief information that may provide certain clues to the topographic expression. Craters *1* and *2* are prominent in the *right panel*, but are almost lost in original photo (a). By *S* marked saturated part of the photograph

## 5 The Surface of Mercury in the Longitude Range 210–285°W. “Skinakas” Basin

The stacked images of Mercury in the 200–290°W longitudes are based on several series of successful observations carried out in early May 2002 at the Skinakas Observatory of the Heraklion University (35°13'E, 24°54'N, Crete, Greece). The same STV CCD camera (with pixel size  $7.4 \times 7.4 \mu\text{m}$ ) mounted on a Ritchey–Chrétien telescope ( $D = 1.29 \text{ m}$ ,  $F = 9.857 \text{ m}$ ) was used. The disk of the planet on May 1 and 2, 2002, was seen, on average, at an angle of 7.75 arcsec with its linear size of 0.37 mm in the focal plane of the telescope and corresponded on the CCD array to only 50 lines in zoom mode, or 25 lines in normal mode (four pixels binned). The phases of Mercury were 93° and 97°. Short exposures, mainly 1 ms and up to 10 ms at large zenith distances, were used. Stable seeing conditions were at the Skinakas observatory on May 1 and 2, 2002; that was a key factor for successfully obtaining a very large number of raw electronic images, about 20,000. Since the size of each image (like those seen in Fig. 15) is only 7.75 arcsec, an image unsteadiness of only 1–2 arcsec would have brought part of the image outside the CCD fragment used.

Images of the surface range in Mercury's longitude 210–285°W were stacked in the course of processing the data set collected during the observations on May 2, 2002. The processing was continuously perfected and became more and more complex. The image resolution and the reliability of identifying the detected relief or albedo features of the planet increased accordingly. The first version of the stacked images from the processing of the 2003 observations was based on the 1,120 raw photographs; about 35% of these remained after manual selection (Ksanfomality 2003). This comparatively rough image (Fig. 18, phase 97°) immediately showed the largest structures in the longitude range 210–285°W, the most prominent of which is the “Skinakas Basin”, considered in the following.

Further substantial progress in resolution was made in 2004. The second version of the image was based on a considerably larger number of primary photographs, 5,240; the photographs used to synthesize the first version of the image were excluded. Figure 19 with the coordinate grid shows the synthesized images of Mercury at phase 97°. It demonstrates how the images improved as increasingly more raw photographs were included in the processing and as the stacking technique itself was perfected. The coordinate identification error

**Fig. 18** The first version of the stacked image of the Mercury's surface in longitude range 210–285°W, based on the data set collected during the observations on May 2, 2002. This is a comparatively rough image, immediately showing Skinakas Basin, the largest complex structure in this longitude range. The phase is 97° (from Ksanfomality 2003)

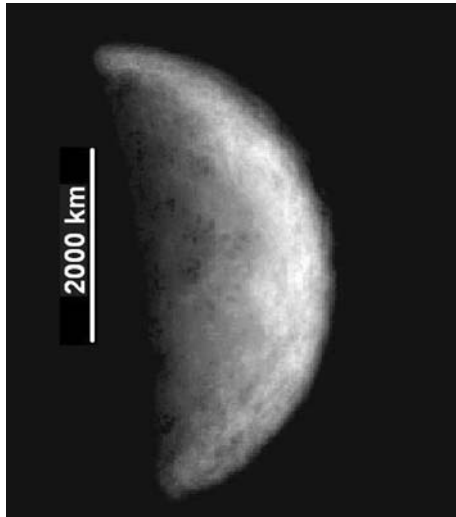
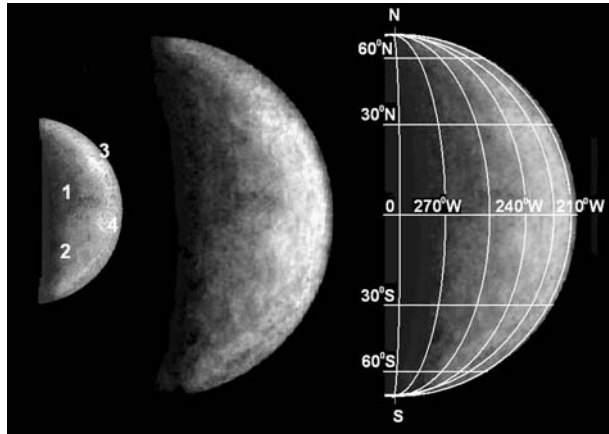


**Fig. 19** Progress in the resolution of stacked images for Mercury at phase 97° (May 2, 2002). The central meridian is 286°W. Images (Fig. 18 and Fig. 19) were synthesized from independent raw data that number 1,120 and 5,240 primary electronic photographs, respectively. Details marked as 1–3 are considered in Sect. 8

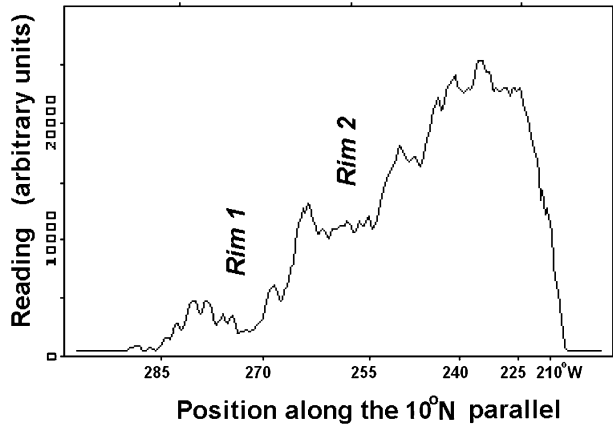


does not exceed a few degrees, but it increases near the poles. The coordinate grid was constructed by taking into account the fact that the North Pole at the time of observations was displaced from the limb toward the observer by a few degrees.

Although all of the large image features are present in both Figs. 18 and 19, the version in Fig. 19 is appreciably sharper. The photometric function was removed more accurately. However, a contrast of large dark areas (like feature (1)) is lost to some extent. Both large and small structures can be distinguished in Fig. 19. An example is a large, about 1,200 km, pentagonal ray crater (2) at 36°S, 260°W, marked only in Fig. 18 but seen well in Fig. 19. Of the same size is a crater centred at 0°, 265°W. The sophisticated image processing resulted in Fig. 19, which allows us to discern similar features that are near the terminator. Details marked as 3–4 are considered in Sect. 8.

In the previous section, in the cases of Figs. 12 and 16, the reality of the results could be confirmed by their comparison with Mariner 10 images. However, what could be a proof that new formations found in the longitude range 210–290°W actually reflect the Mercury's geography? Since details of the planet's surface in this region were unknown, the first and

**Fig. 20** Cross-section of rims of S Basin image along parallel 10°N

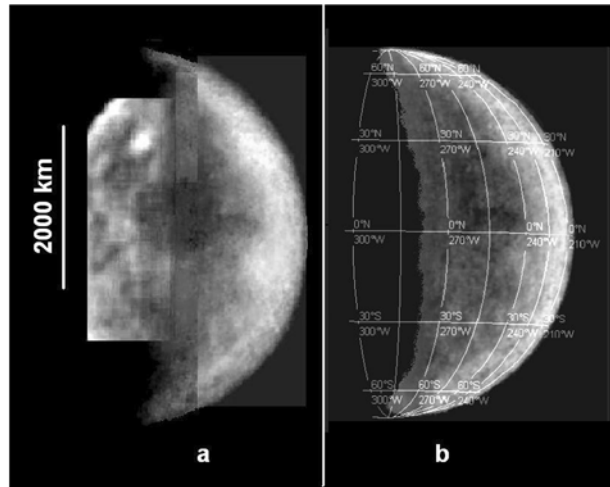


main criterion for the features being real was their presence in several synthesized images acquired independently and based on independent groups of primary electronic photographs (Ksanfomality, 2002, 2004). Using this criterion proved to be the most reliable method for confirming that these features are real. Nevertheless, in two cases, the detected features have been found in independent publications (Harmon et al. 2001; Dantowitz et al. 2000; Baumgardner et al. 2000). These are the formations near the North Pole and the Skinakas, or “S” Basin, respectively.

The most prominent feature (1) in Figs. 18 and 19 is a large, dark “basin” (according to the lunar terminology) near the terminator, centred approximately at 5–9°N, 270°W. The basin, the largest formation in the longitude range 210–290°W, has an inner diameter of about 1,000 km that is more or less regular in shape. The discernible irregular outer rim has twice the diameter of the inner part (Fig. 18). The structure of the inner rim of the basin, according to Fig. 18, is comparatively regular on the eastern side, but its regularity is distorted by an object centred at 35°N, 270°W in the north and by an extensive, lighter region located between 250° and 280°W, extending from 5°S to 25°S in the south. A large, right-angled area extends from 0 to 8°N, from 245 to 262°W and covers an area of 340 × 720 km; it is the darkest spot in this sector at 8°N, 250°W (Fig. 19). It could be a deep bottom-land (examined in Sect. 6).

When processing the observations, the nickname “Skinakas Basin” (after the Observatory where the data were obtained) was used for this formation, without having any pretension to making this legally binding; the IAU is known to name all objects on the surface of Mercury after writers, composers, artists, etc. Nevertheless, the name “Skinakas Basin” (or “Skinakas Mare”) mentioned at several conferences (Ksanfomality 2004, 2005, 2006) has already been accepted in the literature. To avoid this problem here the name “S Basin” is used. In Ksanfomality et al. (2005), the S Basin and Caloris Planitia were compared and it was shown that S Basin is the largest basin on Mercury, about 1.3–1.5 times the diameter of the Caloris Planitia. The basin is probably a very old formation on Mercury, with broken rims that are actually overlapped by the boundaries of other, smaller basins. The morphology of the rims of the basin seems to be similar to that of Caloris Basin, or may resemble more or less the large old formation Aitken-South Pole on the far side of the Moon. The signatures of the rims are clearly seen in Fig. 20, which shows a distribution of brightness across Mercury’s image shown in Fig. 18, along a parallel at latitude 10°, crossing the S Basin from terminator to limb. Distinct rims are seen along the 10° N latitude trace.

**Fig. 21** (a) The composed view of S Basin from images in phases 29.08.1998 (Baumgardner et al. 2000; Dantowitz et al. 2000) and 2.05.2002 (Ksanfomality et al. 2005). (b) Location of coordinates grid

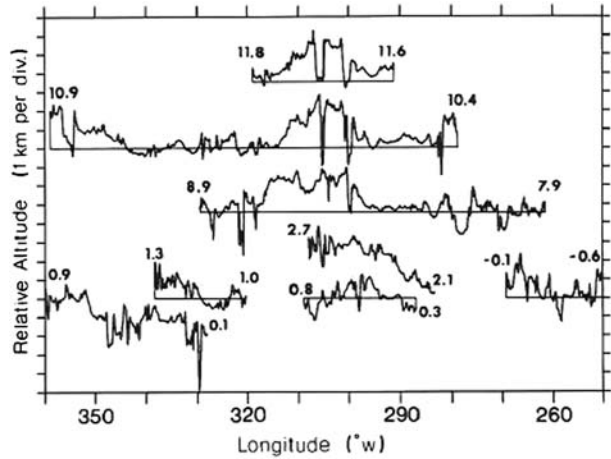


Only the eastern part of the Skinakas Basin is seen in Figs. 18 and 19. Nevertheless, it was possible to compose a full image of the S Basin. For this purpose, the eastern part of the basin was taken from Ksanfomality's data and its western part from the revised results of Dantowitz et al. (2000) and Baumgardner et al. (2000), shown above in Fig. 9c. As was noted in Sect. 3, Dantowitz et al. (2000) and Baumgardner et al. (2000) took numerous electronic photographs of Mercury at phase  $106^\circ$ , in the longitude range  $265\text{--}330^\circ\text{W}$ , on August 29, 1998, using the 60-inch Mount Wilson Observatory telescope. Each of the teams published their results and mentioned the bright object in the upper part of the image ( $35^\circ\text{N}$ ,  $300^\circ\text{W}$ ). In addition, Dantowitz et al. (2000) pointed out that the observed features include an interesting ring object at the terminator, approximately at  $10^\circ\text{S}$ ,  $270^\circ\text{W}$ . Baumgardner et al. (2000) mentioned it also and called this object a large, dark mare-like region at about  $15\text{--}35^\circ\text{N}$ ,  $300\text{--}330^\circ\text{W}$ . In both cases, this position virtually coincides with the position of the centre of the S Basin. Due to a favourable coincidence, the terminator's position is in fact the same as evening terminator in Fig. 9 and morning terminator in Figs. 18 and 19. On this basis, the full image of the Skinakas Basin was constructed. The details are given in Ksanfomality (2006) and Ksanfomality et al. (2005). The favourable location of the S Basin in Figs. 9 and 18 allowed both its halves to be matched.

The results of joining the images of the western and eastern parts of the S Basin are shown in Fig. 21a. In Fig. 21b, the coordinate grid position is shown. Since matching was performed without coordinate transformation, it definitely cannot be exact. However, the limited resolution of the images makes the result quite acceptable even without coordinate transformation. As can be seen from Fig. 21a, the S Basin is a typical crater mare with a dark central part and a periphery of complex structure. The scale of the formation is shown on the left. As was estimated earlier, the sizes of its central and outer parts are about 1,000 and 2,000 km, respectively. The image was not sharp enough: only large features were identified reliably, but their detailed description was waiting for new observations. It is pertinent to note that the vague dark formation denoted by Mendillo et al. (2001) on their scheme coincides in position with the S Basin.

It is interesting to compare the S Basin sizes with the lunar forms. The inner part of the basin slightly exceeds in size the largest lunar Mare Imbrium, while its outer part has the scales of the lunar Oceanus Procellarum. In contrast to the S Basin and Caloris Planitia, the surface of Mare Imbrium is a lava field the formation of which dates back to the ancient

**Fig. 22** Relief scans acquired by Arecibo radar imaging across Mercury crossing the area of S Basin. Latitude is indicated by the numbers at the ends of the scans. Relative altitude is given on vertical scales. From Harmon and Campbell (1988)



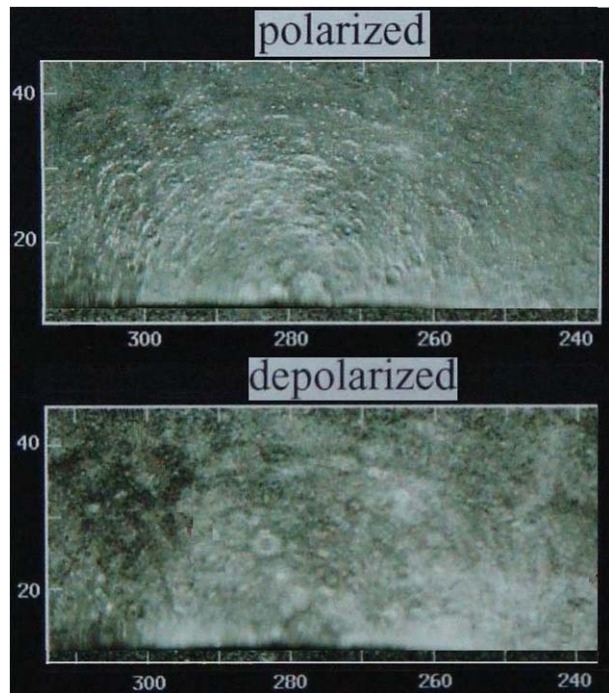
epoch of global lava flows on the Moon. However, it is not quite appropriate to compare the S Basin with lunar mare regions. In general, their albedo is a factor of 2–3 lower than that of the highland area. Since the data processing when Mercury’s images were stacked included the “unsharp mask” operation, the albedo variations are difficult to estimate reliably. If the S Basin is assumed to be actually a broken impact crater, its sizes point to a very large impact event that dates back to the early history of Mercury.

The structure of S Basin is complex, and when studied in detail shows multiple impact features with degraded rims (Fig. 19). There are several complex structures and their relief cross-section may be traced in radar topographic tracks of Mercury’s surface reproduced from Harmon and Campbell (1988) in Fig. 22. The longitude coverage of Fig. 22 includes the longitudes 250° to 300°W. The radar traces in Fig. 22 are labelled with latitude at the ends of the relative altitude traces. Of considerable interest is the trace at 10.4°N latitude which traces a deep depression of 2 km beginning at 277°W longitude and continuing to a maximum depth of 3 km at the rim near 300°W longitude. The same depression structure is traced at latitude 7.9°N at 260°W with an interruption of a degraded rim at 280°W continuing to the next rim at about the same longitude as the trace beginning at 10.4°N.

The dual-polarization, delay-Doppler upgraded Arecibo radar images clearly show the same large, multi-rimmed basin (Harmon 2007). In older radar images the bright region (that has been named “radar bright spot C”, Butler et al. 1993) is an unusual, somewhat chaotic region with clusters of circular features. It coincides with a multi-rimmed basin in the Arecibo images of Harmon et al. (2007). Its northern part is shown in Fig. 23 and is in good agreement with the visible/IR images. There appears to be a large radar-dark albedo section extending from 210° to 300° and from 30°S to 40°N in latitude. The dark region is interrupted by various bright features. The bright semi-circular feature in the centre 8°N between 230° and 250°W could be the inner, less-degraded rim of the huge basin. The centre of the feature is 10°N, 277°W and the diameter of outer rims about 50° (corresponding to 2,100 km).

There are very dark regions in both the visible and radar images. The radar image albedo is highly dependent on terrain roughness on the scale of the wavelength of the observation (12.6 cm). The methods of obtaining visual/IR images of ultrahigh resolution have gradually improved. The best results were acquired at the end of 2006; S Basin was one of main goals. The observational data will need, naturally, more time to be processed, preventing their inclusion in this review. It was only possible to prepare a quite preliminary version of

**Fig. 23** Image of S Basin obtained by Arecibo radar imaging (Harmon et al. 2007). Northern half of S Basin



processed observational data collected on November 21, 2006. These observations are of a special interest as at that time the S Basin was on the sunlit side of Mercury.

In Fig. 24, the position of the S Basin is shown in the right panel by a black circle with the location of the coordinate grid. In the left panel in the centre of the image (and adjusted west to the S Basin centre) is a large crater, with a diameter 500–600 km. On the external rim, more than 1,600 km in diameter, numerous secondary formations are apparently imposed.

The S Basin may be one of the most interesting features in longitude range 210–290°W. Nevertheless, craters of complex structure are frequent on planets and satellites. Among the unique forms on Mercury, some unusual formations found in 2006 have been identified (Ksanfomality et al., in preparation).

## 6 Other Remarkable Features in Longitudes 210–285°W

Figure 25 shows the positions of the most prominent large craters discussed in the following. Evidently all of them are of impact origin. Large craters with extended ray systems are visible in many areas. The best conditions for discerning them are at the terminator of the planet, as contrasts are increased. In Fig. 25 large craters are marked by numbers 1–7. To improve their visibility we place in Fig. 25, together with the initial (b) and gamma-corrected image (c) for the phase 97°, contrasted versions of the fragments, taken from image (b). All craters but (5) have wide debris terraces. The centre of the largest and most noticeable crater (1) is placed at 30°S, 265°W. It has a pentagonal shape and a bright fresh rim of debris blanket. The whole rim formation is estimated to have sizes of 900–1,100 km. The outside rim is probably the excavation debris. About 5° northward of it there is another large crater (2), 700–800 km in size. Feature (3) is a large dark crater (or basin) at 1°S, 265°W at the extreme south border of S Basin with a large, about 1,000 km, rim of debris and a

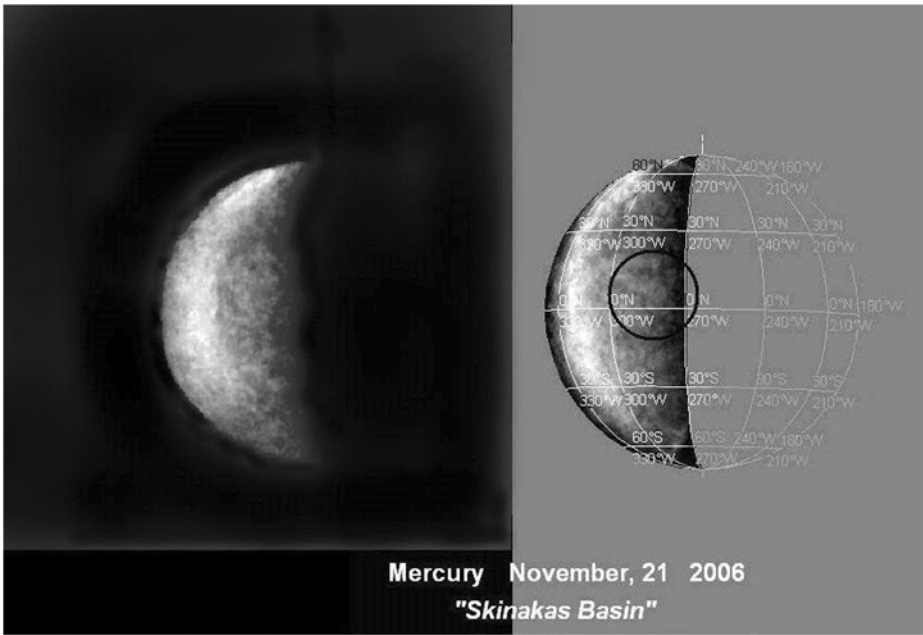


**Fig. 24** Preliminary version of processing of experimental data of November 21, 2006, with S Basin (circled by black ring in location of coordinates grid) placed on lit side of the planet

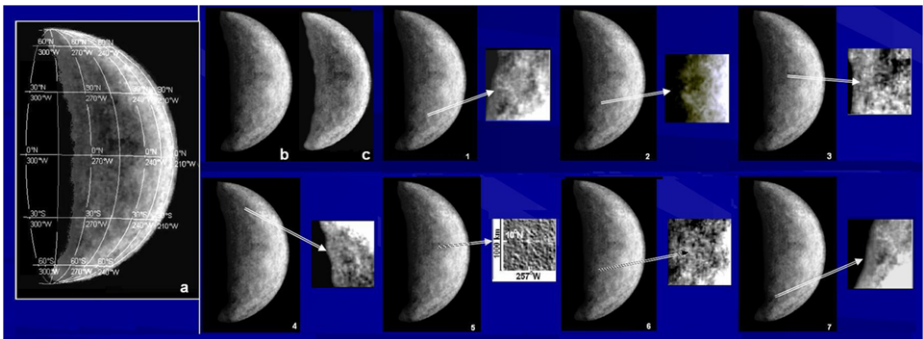


**Fig. 25** Large impact craters, marked by numbers 1–7, are shown, taken from the image (b) of May 2, 2002, for the phase 97°. The gamma-corrected image (c) presents details close to the terminator. Coordinates grid is shown in panel (a). The fragment (5) demonstrates rays from crater 5 acquired by means of high-pass filter. All the fragments are shown in 2:1 scale to the images (b) and (c)

central hill. The centre of feature (4) at 40°N, 275°W is a round, very dark 300-km crater of elongated shape with a size of destroyed outer rim of about 400–500 km. On the east periphery of the S Basin there are separate dark areas with a small dark object (5), about 80 km diameter, at 10°N, 257°W, surrounded with a light blanket of debris, about 200 km. It evidently possesses bright rays, discernable in the fragment 5 made by the high pass filter. The eastern light rays are traced up to 500 km in length. This is probably a young formation. The crater (5) is the smallest. To the west and south of it are extensive dark areas of 400–

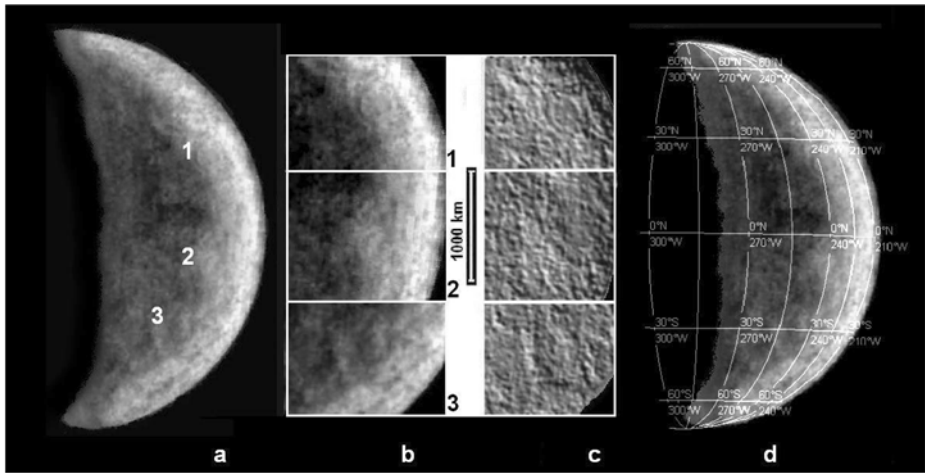


**Fig. 26** (a) Large features at the limb in the longitude range  $210\text{--}290^\circ\text{W}$ , phase  $97^\circ$ . (b) The column of enhanced-contrast fragments. (c) The view of the same areas acquired using a special image processing code. (d) The location of the coordinate grid

600 km in size. The strangest and the largest (about 1,400 km) is the feature (6) centred at  $13^\circ\text{S}$ ,  $265^\circ\text{W}$ . It is a chaotic relief area with few craters, no rim blanket, and the whole area is surrounded by a narrow, thin valley. The crater (7) at  $45^\circ\text{S}$ ,  $270^\circ\text{W}$  has a common part of the rim blanket, with the whole area surrounded feature (1). It has a dark central crater of about 200 km and an outer rim of about 400 km.

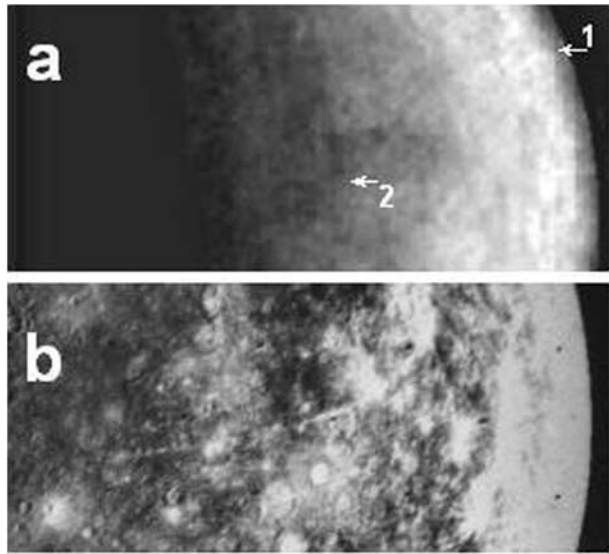
A bright, large (about 900 km) and probably very young crater at  $30^\circ\text{S}$ ,  $210\text{--}220^\circ\text{W}$ , with the extended blanket debris, is placed at the very limb while in  $97^\circ$  phase. It is seen much better in  $93^\circ$  phase image (considered in Sect. 8).

Some ray craters in the segment  $210^\circ$  to  $290^\circ\text{W}$  were considered by Ksanfomality and Sprague (2007). Close to the North Pole, there is a large impact crater at  $85^\circ\text{N}$  with an extensive debris blanket about 280 km in diameter (seen at the very north edge in Fig. 25c). Its central dark part is about 90 km in diameter. The size and position of the crater coincides with a crater K in the radar map (Harmon et al. 2001). The debris blanket on the radar map is seen as a dark belt without details, while in the optical image the debris blanket extends radially and has a higher albedo than the centre of the crater. These differences in albedo may have implications for the surface composition. It has been suggested that volatiles, for which a favoured candidate is water ice, produce coherent backscatter and bright depolarized radar albedo (Slade et al. 1992; Harmon and Slade 1992; Butler et al. 1993). Vilas et al. (2005) measured the depth-to-diameter ratios of the polar craters and found them to be abnormally shallow, supporting the notion that they have an infilling material. It may be that the albedo of the debris from these craters seen in the vis/IR images indicates the presence of unknown material.

Since the gradations of albedo or relief features are small, the possibilities for increasing the contrast are limited: for the same shape of the gamma function, increasing the contrast of some details leads to the suppression of others. Nevertheless the procedure of selective increases in contrast and using a high pass filter reveals numerous interesting features that become apparent at the limb of the segment  $210^\circ$  to  $285^\circ\text{W}$  (Fig. 26).

Very light regions near the limb (1) are placed at  $20\text{--}35^\circ\text{N}$ ,  $220\text{--}235^\circ\text{W}$ . This is the brightest spot in the image of Mercury at phase  $97^\circ$  and at this part of the planet. At first

**Fig. 27** (a) Thin arc-shaped (due to spherical projection) ray is emerging at the limb (*1*), at about 18°N, 210°W, crossing the equator at 260°W (*2*). (b) Another thin arc-shaped ray is seen in Mariner 10 photograph (emerging at about 15°N, 120°W, terminating at equator, 160°W)



look it appears as a young impact crater, but no evidence of ray structure can be found. On contrasted fragment 1 (Fig. 26b) the area appears as a 500–700 km collection of chaotic high albedo sites with a round structure centred at 20°N, 245°W. Additional processing shows that the round feature is a 350-km basin of unusual shape, bordered by two large arcuate valleys of regular shape on both sides (Fig. 26c). The bright round feature (2) in Fig. 26b, centred approximately at 10°S, 230°W, after processing, appears to be a regular basin of lunar type, with a double, partially destroyed rim, about 800 km in diameter. Fragment (3) in Fig. 26b centred approximately at 30°S, 245°W is a huge, destroyed basin with a diameter of 700–800 km and a heavy eroded rim. The entire surface and periphery of the basin consists of a superposition of craters and basins with degraded rims that indicate the antiquity of the feature 3. This type of basin is called “relict circus”, according to lunar terminology.

Besides the huge features described above, stacked images of Mercury (e.g., Figs. 19 and 25) show unusual features on Mercury’s surface. One of them is very thin arc-shaped ray appearing at the limb at 18°N, 210°W, extending for a quarter of the planet and crossing the equator at 260°W. The spatial resolution of the image of the ray (as for a long, linear feature) is about 80–100 km, with its length between marks 1 and 2 being about 1,600 km. As for the arc-shaping, it is due to the spherical projection. The ray is seen well in contrasted images, like Fig. 26a. Another thin arc-shaped ray of this sort is seen in a Mariner 10 photo (Fig. 27). Similar features are known on the Moon, e.g., a ray crossing the Bessel crater at the centre of Serenitatis mare, or rays from the Tycho crater. However lunar rays are not this thin and do not reach this extent. Their origin supposes a huge impact. Keeping in mind that gravity acceleration on Mercury is twice the lunar value, the length of arc-shaped rays in Fig. 27 needs an explanation. Another interesting property of the ray in Fig. 27a is that when crossing the north outline of a large right-angled dark area at 8°N, 250°W, the ray is shifted a bit southward. It could be a manifestation that the dark area is a deep bottom-land. Its extents are 0 to 8°N, 245 to 262°W ( $8 \times 17^\circ$ ), or  $340 \times 720$  km.

Contrasting the images in Figs. 24, 25 and 26 for selection of interesting features in longitudes 210–285°W sector distorts inevitably the original distribution of bright and dark hues over the planet’s surface. Their distribution in a less distorted way is presented in Fig. 19. The eastern part of the extended dark S Basin dominates in this sector.

## 7 High-Pass Filtering Images of Mercury: An Attempt at Restoring Relief Information

It is well known that restoring relief requires stereo images (cf. Cook and Robinson 2000). Is not possible to derive topographic information strictly from a single image, nevertheless, one may try to obtain useful information about topography of the area using a high-pass filter. Conversion of a single half-tone image to a so called “relief image” is a standard option of many image processing programs containing a task called “Relief”. It is obvious that the brightness of a separate detail is defined by the conditions of illumination, the reflective properties (albedo) of the given surface, and its geometry. Retrieving quasi-relief information from the stacked images may provide certain clues to the topographic expression (Ksanfomality 2005). An example of conversion of a single half-tone image to quasi-relief form is illustrated by Fig. 17b (a conversion of a Mariner 10 photo shown in Fig. 17a). The irregularities of basin, craters and ray systems are clearly revealed. Relief of many features, like two large craters 1 and 2 placed close to the limb (not noticeable in Fig. 17a), becomes rich with details. The blind flat area S at the limb is a result of Mariner 10 data saturation. It is easy to see the thin, long arc-shaped ray across the photo, mentioned earlier.

The method was applied to the Mercury pictures using a specialized program. Conversion of the image stacked from primary images of Dantowitz et al. (2000) and Baumgardner et al. (2000), August 29, 1998, Fig. 9c, is presented in Fig. 28a. Limited topographic information appears, e.g., a long valley at the equator. More effective is the conversion of images stacked by L. Ksanfomality for data acquired on November 2, 2003, resulting in Figs. 28b and c. The direction of conditional illumination used for processing was in Fig. 28 from the southwest. Phase effects and shades of grey were suppressed. Comparison of stacked and converted images shows that fine features get underlined and became much more distinct than in the original pictures. More distinct are, for example, the giant round crater in the northeast of Fig. 28b and many other features. The results shown in Figs. 28a and c were presented for the first time at the 2nd AOGS conference (Ksanfomality 2005). In Fig. 28b and c, more detail is apparent than in Fig. 28a, because of the better quality and large number of the initial images. Converted pictures look more informative than original images.

The best result came from processing Fig. 19, May 2, 2002. Here many stacked images and their high quality played a positive role. The result does appear to give topographic information that delineates plausible features over the surface. It is impossible to determine whether explicit features are topographic highs or lows but by analogy to lunar cratered terrain and the side of Mercury imaged by Mariner 10, it is possible to recognize some relief

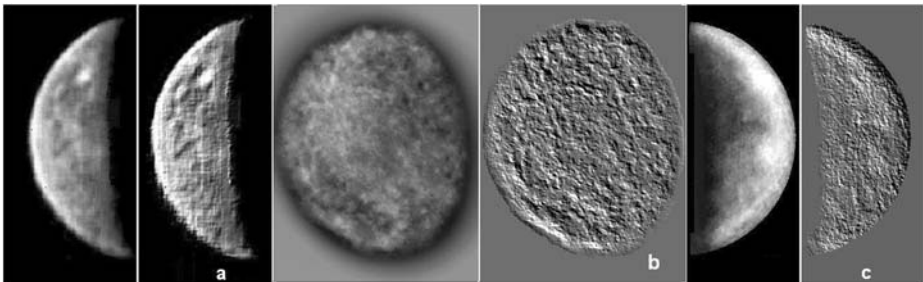


**Fig. 28** It is impossible deriving topographic information from a single image. Nevertheless, one may try to acquire certain clues to the topographic expression using high-pass filter. Examples based on: (a) August 29, 1998 (Fig. 9c); (b) November 2, 2003 (Fig. 16); (d) May 2, 2002 (Fig. 19)

forms. In the left and right part of Fig. 28c the same regions are shown that were marked in Fig. 26. Figure 28c allows some of the estimates given above to be improved. The region of the S Basin is actually a superposition of 500–700-km broken old depressions, similar to crater maria, with central structures, hills or craters. Region 1 resembles a deformed 300–400-km crater mare of complex structure. The crater mare 2 (centred at 10°S, 230°W, diameter of about 700–800 km) with a double rim has the sharpest edges in the longitude sector 220–250°W. A broken large area 1,000 km in diameter with a centre at 13°S, 265°W and a broken double rim is adjacent to it on the west. Depression 3 and other areas are also distinguished. A more detailed geological interpretation of the longitude sector 215–285°W is needed.

## 8 Photometric and Polarimetric Properties of Mercurian Regolith Acquired in Experiments

It is well known from lunar observations that the view of an atmosphereless celestial body changes rapidly as it passes through its quadrature phases. It was interesting to trace the pattern of change in Mercury's view at this favourable phase, especially since, in contrast to the Moon, all sides of the planet are observable in principle at any phase. Unfortunately, only images at two neighbouring phases were acquired, since the observations in May 2002 were limited to only two evenings, May 1 and 2, due to meteorological conditions; the meteorological conditions on May 2 (phase 97°) were appreciably better. The image was stacked from the observations on May 1, 2002 (phase 93°) using more than 7,800 primary photographs. Despite their large number, the image at phase 93° is inferior in feature distinctness to that at phase 97° precisely because of the less favourable meteorological conditions. The observations themselves on May 1 and 2 were performed at the same time of the day. In one day, the subsolar point on Mercury is displaced, on average, by 6° toward the increasing west longitudes, while the phase angle changes, on average, by 4°. Thus, the rate of change in Mercury's phases is half that of the Moon. Two views of the planet, at phases 93° and 97°, are shown in Figs. 29a and b. Figure 29c shows the location of the coordinate grid. Although the phase difference is small and the subterrestrial point in Fig. 29a is displaced rightward, the objects at the terminator are seen much better owing to the earlier phase as, for example, the craters at 45°N, 264°W and 15°S, 270°W shown in Fig. 25. The structural features of the S Basin are seen much better. The large dark area that has not yet reached the limb at phase 93° is located northeast of region denoted 3 in Fig. 19. As regards region 3 itself, its brightness at phase 93° is appreciably lower than at phase 97°. It can probably be concluded from the sharp rise in the brightness of region 3 in Fig. 19, as the phase changes by only 4°, that region 3 is young. The young Tycho crater on the Moon is known to have the same properties. The image of Tolstoj basin (consisting of two photos in Fig. 17) showed the same effect, despite a minor phase difference between the upper and lower photos.

The lightest region near the limb, south of the equator (region 4 in Fig. 19), at this phase is the brightest object on the surface of Mercury. In general, the ring outlines of region 4 are the same as those at phase 97°; its entire structure reaching 1,000 km in diameter appears light, while its western part remains brightest at phase 97°. At phase 93°, region 4 is considerably brighter than region 3 which is the brightest at phase 97°.

One of the known powerful methods used to study physical properties of the regolith is polarimetry. In the observations of 2001 (in autumn morning elongation) an attempt was made to acquire data on the distribution of the degree of polarization of the light over the disk of the planet (Ksanfomality 2002). The data are the same that were used to produce

**Fig. 29** Comparison of views of Mercury at longitude sector 210–285°W in two phases: (a) 93°; (b) 97°

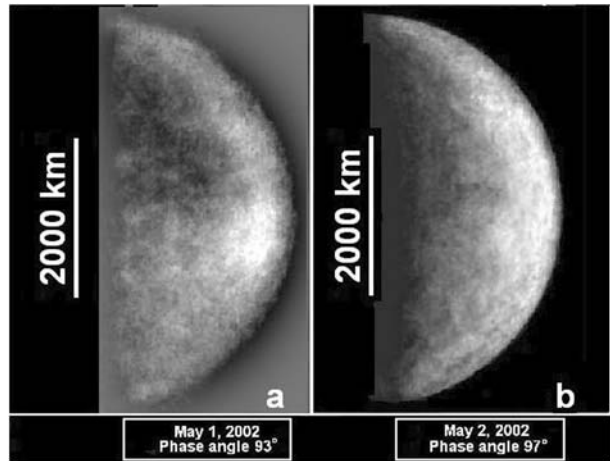
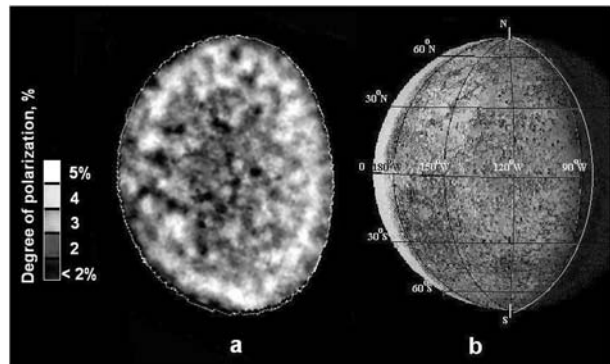


**Fig. 30** Distribution of the degree of polarization of the light over the disk of Mercury at the longitude sector 90–180°W, at 63° phase



the image in Fig. 12, with the same limitation about blurring at the periphery and a high resolution only at the central part of the image. The result is shown in Fig. 30. The range of the degree of polarization was 2.5 to 5%, presented accordingly by dark and light tones.

## 9 Photometric Models and Physical Properties of Mercurian Regolith

Accurate photometric characterization of a surface is required for a number of important applications in planetary science. First of all, the reflectance function of a planetary surface provides information on the surface roughness and the regolith optical properties. It is also needed to accurately compare observations acquired under varying geometries and lighting conditions. In addition, for a space mission, knowledge of this function is required to establish instrument characteristics and to define operational parameters. For example, the bidirectional reflectance distribution function is needed to determine exposure times for the camera system while the zero phase angle reflectance is necessary to size the aperture–laser pulse energy product of a laser altimeter.

## 9.1 Models

In this section, we present the photometric functions most frequently used in interpretation of astronomical observations. If the surface is illuminated by a distant point source, the scattered radiance  $I$  in some direction is proportional to the incident solar irradiance  $\pi F$

$$I = \text{RADF}^* F,$$

where RADF is the radiance factor (e.g., Hapke 1993), which is often denoted as  $I/F$ . If the surface is isotropic and flat, i.e., all directions in the surface plane are equivalent,  $I/F$  depends only on mutual orientation of the surface plane and the directions of incidence and observation, which is described by a set of three angles. They are the phase angle  $\alpha$  (between the direction from the object to the light source and from the object to the observer) and the zenith angles of incidence  $i$  and emergence  $e$ . In astronomical observations, instead of  $i$  and  $e$ , another pair of angles is often used: photometric latitude  $\varphi$  (the angle between the normal to the surface and the scattering plane that contains the source, the object, and the observer) and photometric longitude  $\lambda$  (the angle in the scattering plane between projection of the normal and direction from the object to the observer).

These angles can vary in the following ranges:

$$\begin{aligned} 0^\circ \leq \alpha \leq 180^\circ, \\ 0^\circ \leq i \leq 90^\circ, \quad \alpha - 90^\circ \leq \lambda \leq 90^\circ, \\ 0^\circ \leq e \leq 90^\circ, \quad -90^\circ \leq \varphi \leq 90^\circ. \end{aligned}$$

And two sets of angles are connected with the following relations:

$$\begin{aligned} \mu_0 = \cos i = \cos \varphi \cdot \cos(\alpha - \lambda), \quad \tan \lambda = (\mu_0/\mu - \cos \alpha)/\sin \alpha, \\ \mu = \cos e = \cos \varphi \cdot \cos \lambda, \quad \cos \varphi = \mu/\cos \lambda. \end{aligned}$$

To describe the behaviour of the radiance factor as a function of these angles ( $\alpha$ ,  $i$ , and  $e$  or  $\alpha$ ,  $\varphi$ , and  $\lambda$ ), a number of photometric functions were suggested.

### (a) Lambert function

The Lambert function (Lambert 1760) is represented by a simple decrease of  $I/F$  with  $\mu_0$ , and does not exhibit any specific dependence on  $\alpha$  and  $\mu$ :

$$I/F = A_L \cdot \mu_0.$$

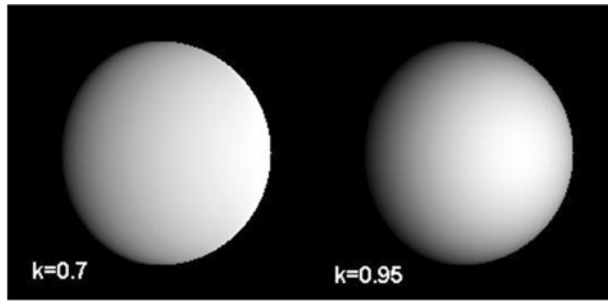
The Lambert albedo,  $A_L$ , is the fraction of incident solar irradiance scattered by the surface into solid angle  $\pi$  (Hapke 1993).

### (b) Minnaert function

The Minnaert function (Minnaert 1941) is the expansion of the Lambert function by introducing an additional term dependent on  $\mu$  as well as the Minnaert coefficient,  $k$ , an empirical constant that sets the weighting between the incidence and emission angle contributions:

$$I/F = \pi A_M \cdot \mu_0^k \cdot \mu^{k-1},$$

**Fig. 31** The distribution of brightness over the disk of a planet with the surface reflecting according to the Minnaert law. Two cases of the Minnaert coefficient  $k$  are shown. The phase angle is  $30^\circ$



where the Minnaert albedo,  $A_M$ , is the fraction of incident solar irradiance scattered normally from a normally illuminated surface. The coefficient  $k$  ranges from 0.5 (for a very rough Moon-like surface) to 1.0 (the Lambert law for a completely orthotropic reflecting surface). The model images below illustrate how the assumed value of  $k$  influences the view of the planetary disk ( $\alpha = 30^\circ$ ). The larger  $k$  (the closer the photometric function to the Lambert one), the stronger limb darkening is observed (Fig. 31).

Special tests of the Minnaert function in comparison with the Hapke function (see below) justified its use for limited angle ranges (Hapke 1981). However, it was shown that the “constants”  $A_M$  and  $k$  are both functions of phase angle.

*(c) Lunar–Lambert function*

A photometric function now known as the Lommel–Seeliger lunar function was derived by Chandrasekhar (1960) from the radiative transfer law to describe the scattering properties of the Moon:

$$I/F = (\omega/4) \cdot \mu_0/(\mu + \mu_0) \cdot f(\alpha),$$

where  $\omega$  is the single-scattering albedo and  $f(\alpha)$  is an arbitrary function describing the phase dependence of the surface radiance factor. For most surfaces observed in the Solar System, a linear combination of this function with the Lambert law, the so-called lunar–Lambert function,

$$I/F = A \cdot \mu_0/(\mu + \mu_0) \cdot f(\alpha) + B \cdot \mu_0$$

was found to provide a better agreement with the data than the Minnaert law and was used to study the photometric properties of various planetary surfaces and laboratory samples (e.g., Squyres and Veverka 1981; Buratti and Veverka 1983; Gradie and Veverka 1984; McEwen 1991; Pappalardo et al. 1998; Geissler et al. 1999). The fit which can be obtained with this function is as accurate as that provided by Hapke’s photometric function considered below.

*(d) Akimov empirical function*

To approximate the measured brightness of the lunar disk, Akimov (1979, 1988) proposed an empirical expression, which contains two free parameters,

$$\frac{I}{F} = A \cdot \frac{\exp(-\eta\alpha) \cdot \cos(\alpha/2) \cdot (\cos \varphi)^{\nu\alpha+1} \cdot [(\cos(\lambda - \alpha/2))^{\nu\alpha+1} - (\sin(\alpha/2))^{\nu\alpha+1}]}{1 - (\sin(\alpha/2))^{\nu\alpha+1}} \times \sec \varphi \cdot \sec \lambda,$$

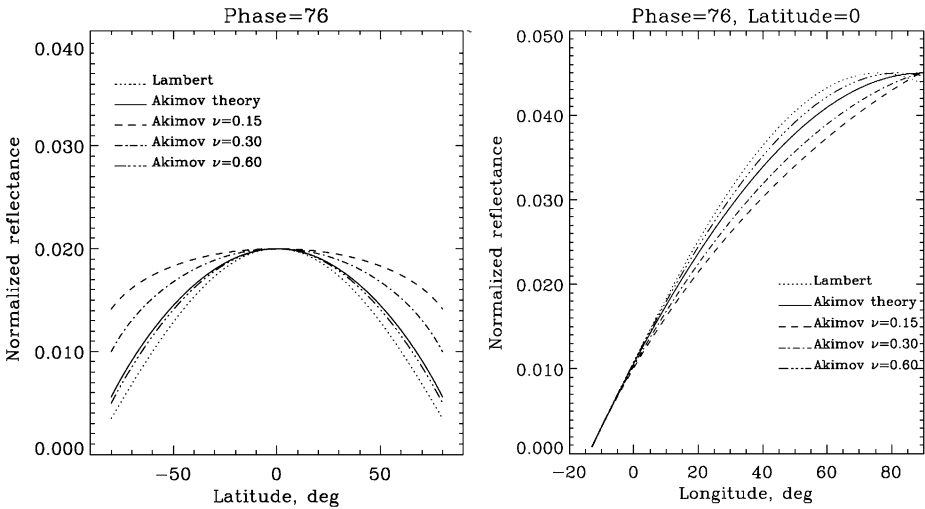


**Fig. 32** The examples of the central meridian and luminance equator disk profiles calculated with the Lambert and Akimov photometric functions for the same phase angle as the profiles measured for Mercury (see below) and normalized to the same maximal value

where  $\eta$  determines the slope of the phase dependence and  $\nu$  (the roughness parameter) averages approximately 0.16 to 0.31 for maria and highlands, respectively. This formula was also successfully used in the analysis of the images of different lunar regions obtained during the Clementine mission (Kreslavsky et al. 2000).

*(e) Akimov theoretical function*

Another approach in finding the reflectance law of the regolith surface is based on the condition that the loose particulate surface being slightly randomly undulated should have the same photometric function as before undulations (Akimov and Kornienko 1994). In this case, the formula obtained for the brightness of the area of the observed planetary disk contains only geometrical parameters and the surface albedo:

$$\frac{I}{F} = A \cdot \exp[0.5 \cdot (1 - 0.5\lambda_{00})] \cdot (\cos \varphi)^{\pi/\pi-\alpha} \cdot \cos\left[\frac{\pi(\lambda - \alpha/2)}{\pi - \alpha}\right] \cdot \sec \varphi \cdot \sec \lambda,$$

where  $A$  is the surface albedo and

$$\lambda_{00} = \frac{\pi}{\pi - \alpha} \cdot \left(\frac{\pi}{\pi - \alpha} + 1\right).$$

This formula, applied to the Clementine images of the Moon, produces a reasonable agreement with the data, though worse than that of the Akimov empirical formula (Kreslavsky et al. 2000).

Figure 32 illustrates the difference between the models and the influence of the roughness parameter of the Akimov empirical function with the examples of central meridian and luminance equator disk profiles. These profiles are calculated for the same phase angle as those measured for Mercury (see below) and normalized to the same maximal value. It is seen that the larger the roughness parameter the closer the profiles to the Lambert one. The

smaller values corresponding to the lunar maria result in much flatter latitude cross-section and produce no limb darkening.

(f) *Hapke function*

The empirical photometric functions described above are useful for providing photometric corrections to data. However, photometric observations also provide important information about the nature of the surface. Extraction of this information requires a more sophisticated model whose parameters are more directly related to the properties of the surface. One such model is an approximated analytic radiative transfer model developed by Hapke (1981, 1993, 2002), which has been shown to accurately fit data from a wide variety of planetary surfaces and laboratory samples (e.g., Helfenstein and Veverka 1987; Hillier et al. 1994; Domingue et al. 1997; Guinness et al. 1997; Johnson et al. 2006).

Hapke's photometric model (Hapke, 1981, 1984, 1986, 1993) (without taking into account the coherent backscattering) is given by

$$\frac{I}{F} = \frac{\omega}{4} \frac{\mu_0}{\mu_0 + \mu} \{ [1 + B(\alpha, h, B_0)] P(\alpha) + [H(\mu_0)H(\mu) - 1] \} S(\alpha, \bar{\theta}),$$

where the factors  $[1 + B]P$  and  $[H(\mu_0)H(\mu) - 1]$  account for the singly and multiply scattered light, respectively.  $P$  is the single particle phase function; the function  $B$  accounts for the shadow hiding opposition effect; the parameters  $h$  and  $B_0$  describe the angular width and amplitude of the opposition surge, respectively;  $H$  is Chandrasekhar's  $H$  functions, which approximate the multiple scattering as isotropic. Later, the assumption on isotropic multiple scattering was relaxed by a special term and the improved approximation for the  $H$ -functions was introduced (Hapke 2002). Finally,  $S$  is a function to account for shadowing caused by macroscopic roughness (Hapke 1984). It incorporates one parameter,  $\bar{\theta}$ , which describes the average slope angle of subresolution topographic relief.

Use of Hapke's functions has the advantage of producing a common framework in which to analyze observed data. On the other hand, it is becoming increasingly clear (e.g., Gunder-son et al. 2006) that extrapolation of Hapke's function is unreliable and hence a complete data set is needed to produce a Hapke fit which can then be used as a predictor by interpolation. Nonetheless, several authors have fit Hapke's model to Mercury's visible phase curve data (e.g., Veverka et al. 1988; Domingue and Hapke 1989; Mallama et al. 2002; Warell 2004) although here too there are inconsistencies between the particular implementation of the Hapke relations used which make intercomparisons between results difficult.

## 9.2 Application of Models to Mercury

The scattering properties of Mercury's surface were previously addressed by Veverka et al. (1988), and many aspects of that work remain appropriate in the absence of additional data. Hapke, in his series of papers, has often used measurements of Mercury's integrated reflectance made by Danjon (1949) to illustrate the fit of his models to observational data (e.g., Hapke 1984).

Extraction of the scattering properties from the Mariner 10 imaging data is hampered by the lack of phase angle coverage (limited to  $90 \pm 10^\circ$ ) and the absence of accurate calibration. Hapke (1984, 1993), however, applied his model to the Mercury brightness profiles measured by Mariner 10 and estimated the model parameters fitting the observed longitude and latitude cross-sections of brightness. They are:  $\omega = 0.25$ ,  $\bar{\theta} = 20^\circ$ ,  $P(\alpha) =$

**Table 1** Hapke parameters fit to the disk-integrated data from Mallama et al. (2002)

Symbol	Value
$\omega$	0.20
$h$	0.065
$B_0$	2.4
$b$	0.20
$c$	0.18
$\bar{\theta}$	16°

$1 + 0.579P_1 + 0.367P_2$  (where  $P_1$  and  $P_2$  are the first and second Legendre polynomials, respectively). In this case the measurements were made far from opposition ( $\alpha \approx 77^\circ$ ), which allows the parameters accounting for shadow and coherent opposition effects to be assumed negligible. Whilst some work is continuing on the Mariner 10 data, there are unlikely to be major developments in the near future. Fortunately, however, there have been other observations (both ground-based and space-borne), laboratory work, and improved modeling work.

An important contribution from imaging observations in advancing our knowledge of Mercury is photometrically calibrated data, used in light-scattering models to derive information of macrophysical and optical properties of the surface. In this respect, both integral disk and disk-resolved image data are important separately and in conjunction, particularly if the phase angle coverage is extensive.

The most comprehensive disk-integrated data set is that of Mallama et al. (2002). Their data set was acquired in the V band with a small telescope and complemented with transformed magnitude observations from the SOHO LASCO spectrograph to cover a very extended phase angle range of 2–170°. It represents the first major achievement of its type since the work of Danjon (1949) who made visual measurements of Mercury's brightness for the range 3–123°. The Hapke parameter fit, using the Hapke (1986) formulation, derived by Mallama et al. is shown in Table 1.

Mallama et al. (2002) determined the geometrical albedo as  $0.142 \pm 0.005$ , which is at the upper end of previously published values, while the estimated average surface macroscopic roughness,  $\bar{\theta} = 16^\circ$ , is at the lower end. Thanks to the coverage of small phase angles, it was possible to study the opposition effect with a higher precision than previously possible, and the brightness was found to surge by 40% from 10° to 2° phase angle. However, the phase curve still does not extend to small enough angles to determine the magnitude of the narrow peak of the opposition surge caused by the coherent backscatter effect. For this information, opposition geometry measurements are needed, which will likely be provided by the MESSENGER Mercury orbiter.

The photometric properties of Mercury compared with the Moon was studied by Warell (2004), based on the phase curve of Mallama et al. (2002) and the highest-resolution SVST images of Warell and Limaye (2001). The improved model of Hapke (2002) was used. Typical results of fitting the Hapke photometric model (lines) simultaneously to observational data for Mercury (red dots) in the form of central meridian and luminance equator disk profiles (left and central panels, respectively) and the Mallama et al. (2002) integral phase curve (right panel) for varying values of  $\bar{\theta}$  are shown below. These profiles are for the 550 nm image obtained at the phase angle of about 76° (Fig. 33).

Similar to the work of Mallama, a small photometric roughness was determined from the integral phase curve data. A value of 8° fits best the observations at high phase angles, but considerably larger values were found to satisfy both integral and disk-resolved data if the

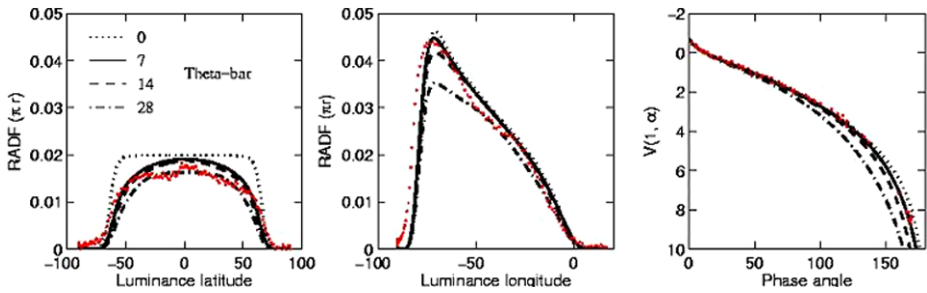


**Fig. 33** Fitting the central meridian and luminance equator disk profiles (*left and central panels*, respectively) and the integral phase curve (*right panel*) observed for Mercury (*red dots*) with the Hapke photometric model (*lines*) for varying values of the parameter  $\bar{\theta}$ , which describes the average slope angle of subresolution topographic relief

phase angle coverage was restricted to moderate phase angles. This was explained as due to contribution of light from predominantly smooth plains units in the highest phase angle data from SOHO, which were determined to imply a surface roughness parameter of about  $8^\circ$ , about twice that of the average Mercurian surface with scattering from all types of geologic units combined. The single-particle scattering function was parameterized with the double Henyey–Greenstein representation, and it was found that the average Mercurian surface was more similar to lunar maria than to lunar highlands. These two observations indicate the possibility that Mercurian smooth plains units are more similar to lunar maria than lunar highlands in both textural and scattering properties. Note that a rather flat latitude cross-section and a weak limb darkening seen in the Mercury profiles comparing to the empirical model by Akimov also indicate a more probable similarity of the Mercurian regolith with that of the lunar maria.

The backscattering efficiency of the Mercurian surface is greater than that of the Moon, possibly due to a high density of internal scatterers in complex agglutinate-rich particles formed from strong maturation processes. In comparison to the Moon, the average brightness of Mercury was found to be 10–15% fainter in the V band based on the integral phase curve, which is supported with historical determinations of the geometric albedos of the two bodies.

While measurements of Mercury at zero phase are impossible from the ground, the results of this fit, and in particular the value of the  $B_0$  parameter, indicate that the opposition effect for Mercury's surface is comparable to or even stronger than that of the Moon. This is critical for laser altimetry which observes, by definition, at zero phase. It is possible that the effect is even stronger than observed by Mallama et al. because the finite angular diameter of the Sun ( $1.1^\circ$  to  $1.7^\circ$  in diameter) would tend to smear out the magnitude of the effect when compared to point source illumination (such as that provided by a laser). Extrapolation of the fit leads to a normal albedo ( $= \pi I(\alpha = 0, e = 0, i = 0)/F$ ) of 0.12 at V band (550 nm) wavelengths. Correlation between parameters in the Hapke fit suggests that interpretation and extrapolation of other parameters should be treated with caution (Gunderson et al. 2006).

Sprague et al. (2004) showed that the spectral slope at visible wavelengths increases linearly with wavelength to first order. Assuming that this finding can be extrapolated to small scales and that the shape of the bidirectional reflectance distribution function curve is not wavelength dependent over this limited range, a normal albedo of between 0.23 and 0.31 can be expected at 1,064 nm (the wavelength of the Nd:YAG lasers to be used for altimetry by

the MESSENGER Laser Altimeter, MLA, and the BepiColombo Laser Altimeter, BELA). The constancy of the BRDF with wavelength is not obvious but has recently been verified over a limited wavelength range (Gunderson et al. 2005).

The surface contrast which will be evident to the MESSENGER and BepiColombo spacecraft has been estimated by Warell and Limaye (2001). Defining surface contrast as

$$\Gamma = \frac{I_B - I_D}{I_B} \cdot 100\%,$$

where  $I_B$  and  $I_D$  are the observed intensities of bright and dark areas, respectively, values of  $\Gamma$  of  $\sim 50\%$  at 550 nm were found.

Reviewing the above models for their applicability, it can be concluded that the selection of the optimum model to use in any particular case will require a further evaluation of the observations and their specific conditions.

## 10 Summary of Results from Imaging and Photometry: Composition and Structure of the Regolith

Ground-based imaging, photometric and polarimetric studies have made it possible to draw a range of conclusions regarding the composition and microphysical state of Mercury's surface.

In terms of the microphysical properties of the regolith, the small radar cross-section, the presence of a negative branch of polarization and the angular location of the maximum polarization value indicate a highly porous regolith similar to the Moon's (Mitchell and de Pater 1994; Dollfus and Auriere 1974). This is supported by photometric studies of the opposition effect of the integral phase curve (Mallama et al. 2002; Warell 2004), though observations at the smallest phase angles ( $< 2^\circ$ ) indicative of the coherent backscattering effect are naturally lacking. Relative brightness variations across the disk in microwave imaging data indicate that the density of the regolith increases from about 1 g/cm<sup>3</sup> in the top few cm to about 2 g/cm<sup>3</sup> at a depth of about 2 m, with a concomitant increase in thermal conductivity (Mitchell and de Pater 1994). The optically active grain size is likely smaller than the case for the Moon (Dollfus and Auriere 1974), and values of around 30  $\mu\text{m}$  have been determined (Sprague et al. 2002; Warell and Blewett 2004).

The scattering properties are generally lunar-like, but a stronger backscattering efficiency and dependence of colour on geometry may be related to a greater abundance of translucent complex glass-rich agglutinate particles (Warell 2004). The backscattering anisotropy, i.e., the amount of light backscattered to the observer, increases with wavelength both in the optical and near-infrared range and the throughout mm–cm wavelengths. In the latter case this effect is manifested in a decrease of microwave opacity with wavelength (Mitchell and de Pater 1994).

The average particle angular scattering function corresponds more closely to that of lunar maria than highlands which would indicate a surface macrophysically more similar to the former lunar terrain. An average photometric roughness of  $20^\circ$  has been derived from photometric modeling of VISNIR and thermal infrared spectra, but regional extents of smooth plains may have smaller surface roughness values of about  $10^\circ$  or less (Emery et al. 1998; Sprague et al. 2000; Mallama et al. 2002; Warell 2004). The absolute V-band brightness of Mercury is 10–15% less than nearside Moon, but considering the more strongly sloped Mercurian spectrum, the “bolometric” average VISNIR reflectances are probably similar

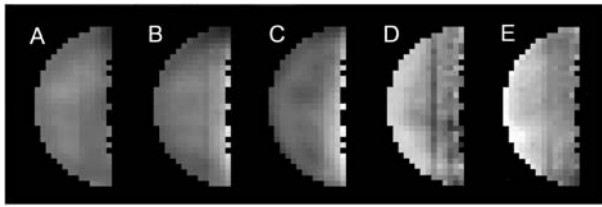


**Fig. 34** Mercury's surface from 210° (limb) to 270° (terminator) W longitudes which is part of the poorly known hemisphere, analyzed with the Lucey method to map varying chemical composition. From left to right, images represent relative 750 nm optical albedo (A), optical maturity + ferrous iron content (B; brighter = less mature or lower iron), titanium abundance (C; brighter = more titanium), ferrous iron abundance (D; brighter = more iron), and degree of optical maturity (E; brighter = less mature). Adapted from Warell and Valegård (2006)

(Warell 2004). Optical photometric and polarimetric data indicate a refractive index of 2.1 compared to 1.8 for Moon, possibly due to the presence of metallic iron particles larger than the wavelength (Hapke 1993).

Compared to the Moon, the microwave dielectric loss tangent is about twice as small as for lunar maria, and 40% less than for the lunar highlands, indicating a surface low in opaques with FeO + TiO<sub>2</sub> around 1 wt% (Mitchell and de Pater 1994). This is supported by compositional modeling of the VISNIR spectrum (Warell and Blewett 2004). One possible explanation is effective secondary differentiation, aided by a high surface gravity, by density-driven plagioclase flotation in magma ocean resulting from a giant impact during the late phase of planetary accretion.

A subset of the images obtained by Warell and Limaye (2001) were analyzed by Warell (2002) in an attempt to study colour variations due to compositional variations on the surface. Individual sharp images of the poorly known hemisphere (longitudes 160–340 degrees) with a spatial resolution of 300 km or higher at four wavelengths from 550–940 nm were ratioed to each other to accentuate relative differences in flux. Of particular interest were the ratios of the 940 nm to the 550, 650 and 750 nm images, for which correlated variations might indicate abundance variations in ferrous iron-rich mineralogy. However, no such deviations were found, and a limit of 2% maximal differences in flux relative to the average was determined. Thus, the variations in mafic compositional abundances of the uppermost scattering surface of the regolith was found to be very small compared to the variation in albedo at a comparable spatial scale, though local variations greater than this limit, present at more local scales, could not be excluded.

A related study was performed by Warell and Valegård (2006) on the basis of new images of Mercury for the longitude range 210–270 degrees, obtained with the upgraded 1-m Swedish Solar Telescope. These images were acquired with basically the same system as used with the SVST. Substantial benefits were available with the new system: chromatic aberration and atmospheric dispersion were completely corrected. For each of six wavelengths from 450 to 940 nm, sharp images were aligned and averaged to increase the signal-to-noise ratio, and ratioed to each other to study variations of colour on the surface. Removal of the photometric function with the theory of Hapke (2002) and extension of methods developed for the Moon (Lucey et al., 2000a, 2000b) to determine abundances of FeO, TiO<sub>2</sub> and degree of maturation, allowed determination of the relative variations of these parameters across the observed hemisphere. With this data set, regional colour variations on disk was detected (Fig. 34) and were found to vary less than the case for the Moon, indicating a surface similar to the lunar farside. Highly reflective albedo features were found to be generally immature, have low to intermediate abundances of opaque minerals and intermediate

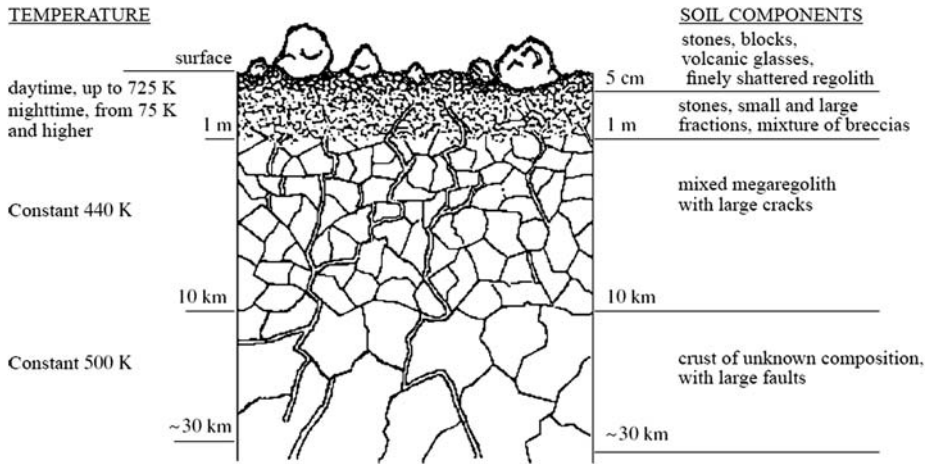
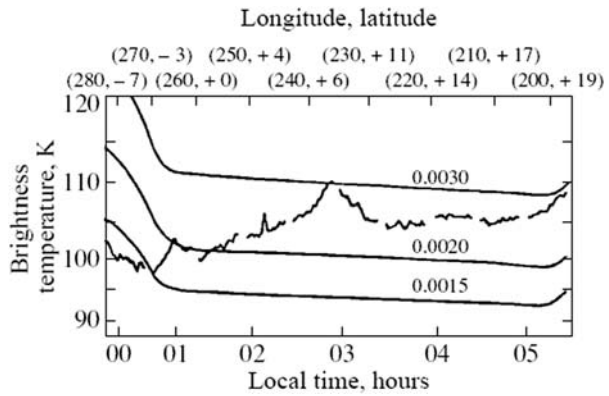


**Fig. 35** Structure of Mercury's surface, according to Sprague et al. (1990)

abundances of ferrous iron. This is consistent with such features being bright immature ray systems of geologically young craters. The very darkest areas in reflectance have intermediate maturities, intermediate to high opaque mineral abundances and intermediate ferrous iron abundances. These may correspond to localized regions of more opaque materials than is typical for the general Mercurian surface, perhaps derived by local extrusive processes from crustal plutonic sources. Generally, Mercury's poorly known hemisphere and the hemisphere explored by Mariner 10 were shown to be very similar, which indicates that if the geologic units are of the same type as on the Mariner 10 hemisphere, they are also likely to have similar areal occurrence globally. Differences in the  $\text{TiO}_2$ -sensitive parameter across the disk were found to be substantially greater than the case for the FeO sensitive parameter, which may indicate that the abundance variations in opaque elements is greater than that of ferrous iron.

A schematic view of the physical structure of a layer of Mercury's regolith to a depth of 30 km is given in Fig. 35. This scheme was proposed by A. Sprague to explain the mechanisms of nighttime accumulation of Na and K in the regolith, with subsequent release of these elements into the atmosphere in the daytime (Sprague et al. 1990). On the surface, along with the finely shattered, sufficiently dry regolith, there are large blocks and stones. The share of glasses of volcanic origin should be low. By analogy with the Moon, it can be expected that the regolith of Mercury was also completely reprocessed in impact processes over geological time. Depending on the local features of the regolith composition, the mean density  $\rho$  falls within the range from 2.7 to 3.2  $\text{g cm}^{-3}$ . The mean value of the thermal inertia  $(k\rho c)^{1/2}$  is close to 0.0025  $\text{cal cm}^{-2} \text{s}^{-1/2} \text{K}^{-1}$ ; i.e., it is much lower than the lunar value. The probing of the lunar crust has shown that, at depths from 1.5 to 30 km, the megaregolith represents a medium scarred by micro- and macrocracks. It is assumed that the megaregolith of Mercury has a similar structure. The maximum temperature (725 K) indicated in Fig. 36 refers only to the specific areas indicated above, while the night temperature (75 K) is observed only in the areas with the lowest thermal inertia, no more than 0.0012  $\text{cal cm}^{-2} \text{s}^{-1/2} \text{K}^{-1}$ , and only in the layer with a thickness less than 1 m. On the average, nighttime temperatures are close to 100 K and the diurnal/annual (176 days) thermal wave does not penetrate to depths greater than 1 m. Below this level, a constant temperature of about 440 K is established. The thermal gradient for Mercury's crust is estimated to be

**Fig. 36** Regions exhibiting differences in the coefficient of thermal inertia (and, perhaps, density) along the track of Mariner 10 measurements (Chase et al. 1974). The coefficients of thermal inertia, equal to 0.0015 and 0.0030 cal cm<sup>-2</sup> s<sup>-1/2</sup> K<sup>-1</sup> correspond, respectively, to lunar-like porous rocks and consolidated rocks



2 K/km. A temperature of about 500 K should correspond to a depth of 30 km. Due to the shattered surface and cracks going down to a large depth, the influx of Na and K to the surface should be stable. The mean value of the dielectric constant  $\epsilon$  at centimeter wavelengths comprises 1.8 in the surface layer (a few centimeters in thickness) and attains 2.9 at a depth of several meters.

According to the results of observations at centimeter wavelengths (from 1.3 to 6.2 cm) obtained by Mitchell and de Pater (1994), the temperature gradient of subsurface regolith layers can locally deviate upward or downward from the predicted value at equal values of the thermal inertia, calculated by a one-dimensional model of temperature diffusion into a depth  $x$  in the regolith layer. We should recall the specific features of the thermal model. The factor of thermal inertia for the regolith is defined as  $I = (k\rho c)^{1/2}$ . Here,  $k$  is the heat conductivity (which is a function of temperature),  $c$  is the heat capacity, and  $\rho$  is the density of the material. The model is built on the basis of the balance of three processes: (i) the absorption of solar radiation  $E(1 - A)/a^2$  by a body with albedo  $A$  moving in the orbit with the semimajor axis  $a$ ; (ii) the intrinsic thermal emission  $\epsilon\sigma$  from the surface having the temperature  $T_s$  and the emissivity  $\epsilon$  and the Stefan–Boltzmann constant  $\sigma$ ; and (iii) the heat influx/outflux  $F_s$  in the vertical direction  $x$ . The balance is determined by the three equations (Ksanfomality 2001):

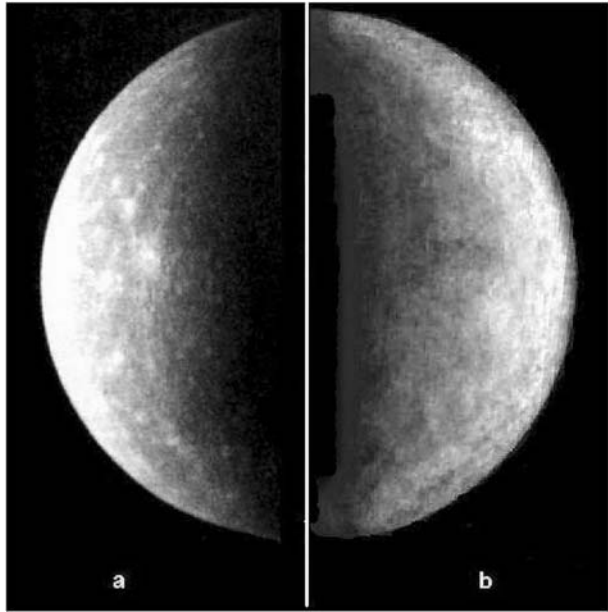
$$\frac{\partial}{\partial x} \left[ k \frac{\partial T(x, t)}{\partial x} \right] = \rho c \frac{\partial T}{\partial t},$$

$$\epsilon\sigma T_s^4 = E_{\odot}(1 - A)/a^2 + F_s,$$

$$F_s = -k \left[ \frac{\partial T(x, t)}{\partial x} \right]_s.$$

A simultaneous solution of these equations enables one to find the value of the thermal inertia factor  $I = (k\rho c)^{1/2}$  for the regolith. The brightness temperature  $T_b$  of Mercury’s surface was estimated from the measurements in the range of 45  $\mu\text{m}$ , which were made in 1974 along the Mariner 10 measurement tracks (Chase et al. 1974). Figure 36 shows the results of these measurements performed in the radiometer channels at 45 mm above the nightside of the planet in the equatorial region, from 23:40 to 05:30 of the local time. The brightness temperature  $T_b$  along the track varied from 98 to 110 K. The temperature  $T_b$  is determined by the thermodynamic temperature of the body  $T_s$  and by the emissivity  $\epsilon$  as  $T_b = T_s(\epsilon)^{1/4}$ . Since  $\epsilon < 1$ , the temperature  $T_s$  is several degrees higher than  $T_b$ . The comparison of the

**Fig. 37** The image taken by the Mariner 10 in 1973 from a distance of about 1 million km (a) and the part of Mercury for the longitudes 210–285°W by ground-based observations (b, phase 97°)



measured temperature with the model determined by three equations shown above made it possible to estimate the thermal inertia factor for the surface rock. In the case of Fig. 37, this factor was found from  $0.0017 \text{ cal cm}^{-2} \text{ s}^{-1/2} \text{ K}^{-1}$ , i.e., somewhat higher than typical values for the Moon, up to  $0.0030 \text{ cal cm}^{-2} \text{ s}^{-1/2} \text{ K}^{-1}$ ; this value corresponds to a sufficiently consolidated rock whose density reaches  $3 \text{ g cm}^{-3}$ .

Sprague et al. (2000) obtained the first infrared images of Mercury's surface in the wavelength region of thermal emission from the surface, for the longitude range 210–250°W. They acquired data at 22 wavelengths from 8.1 to 13.25  $\mu\text{m}$  with the Mid-Infrared Array Camera on the 2.2-m reflector at the Steward Observatory. A large number of 50 ms long exposures at each wavelength were coadded to achieve an angular resolution (0.9–1.4'') at or near the diffraction limit at all wavelengths. Individual coadded images, selected at wavelengths of known emission features in the spectra of terrestrial rocks (augite, diopside, Fe-rich olivine and labradorite), were ratioed to other wavelength images in order to search for contrast differences caused by rock abundance variations across the visible disk. At the angular resolution attained and the pixel scale (0.67'') used, however, it was not possible to detect any flux variations on the surface. Any such variations resulting from compositional variations on the disk were estimated to deviate less than 5% in flux from the surroundings at spatial scales of 700 km.

Concluding this overview of ground-based observations of Mercury, it is interesting to compare the obtained resolution of images of the planet with the Mariner 10 photographs as a whole. This comparison is shown in Figs. 37a and b. Although the longitudes are completely different, the similarity between the views of the surface is very convincing. The stacked image (Fig. 37b) roughly corresponds in resolution to the photographs taken by the Mariner 10 camera from a distance of 1 million km (Fig. 37a). The large dark areas in the new images cover an essentially larger area than can be distinguished in Fig. 37a. In general the view of the Mercurian hemisphere in the longitude range 15–190°W known from Mariner 10 photographs differs markedly from the planet at phase 97° for the longitudes 215–290°W (Fig. 19b), where larger dark regions are located. At the same time, the images

of Mercury more closely resemble the first quarter of the Moon than the widely known and often published mosaic of Mariner photographs.

Ground-based telescopic observations ( $D = 1.2\text{--}1.5$  m and  $D/F = 1/10\text{--}1/20$ ) made with short exposures and with modern image processing, permit us to acquire previously unattainable resolution of Mercury's surface, about 80 km and less. For this, an extended data base, computer programs and high-quality observational material are required. The PSF (point spread function) should be used at a level of 0.85–0.90, instead of the usual 0.7. The image quality and presence (or absence) of small details permit choosing the level of processing. It is also worth mentioning that a technique to retrieve relief has been applied to different images, including the newly processed images in this paper. The result is promising with many features becoming visible and having the appearance of crater rims, central pits, scarps, depressions and hillocks.

## 11 Hypothesis on Possible Connection of the Magnetic Field of Mercury with S Basin

Here we suggest and discuss the hypothesis that the S Basin on Mercury (Ksanfomality 1998a, 1998b; Ksanfomality et al. 2005) can be associated with the measurable magnetic anomaly of crustal origin. The measured global magnetic asymmetry of the planet (Connerney and Ness 1988) can be related to the existence of the S Basin according to this hypothesis. We demonstrate that available knowledge about Hermean magnetic fields (Wicht et al. 2007) does not contradict this hypothesis. We indicate possible directions of search for correlations between magnetic fields and surface properties in complex multidisciplinary experiments onboard future spacecraft missions.

The Mariner 10 measurements (Connerney and Ness 1988) put only some upper limits on small-scale residual crustal magnetic fields, which appear to be of the orders of several nT to several tens nT on average on the length scales and of the orders of several tens to hundreds km on the charted Mercury surface beneath the Mariner's third flyby. It is not clear if such small residual crustal magnetization is typical for the whole planet or only for the investigated region. It is also not clear if stronger crustal magnetization exists and contributes to the global dipole and other harmonics. Only future measurements can clarify the situation.

### 11.1 Introduction to the Hypothesis

The main magnetic field of Mercury is poorly known. Our current knowledge is based on the interpretation of the limited in situ observations during two flybys of the Mariner 10 spacecraft on March 29, 1974 (I flyby) and March 15, 1975 (III flyby) on the nightside of the planet at altitudes above 707 and 327 km, respectively (Ness 1978; Ness et al., 1975a, 1975b). Flyby II was too distant from the planet for this purpose. Magnetic-field observations made during Mariner 10's third encounter with Mercury were interpreted such that an active dynamo is a more likely candidate than fossil magnetization for the origin of the field (Ness et al. 1976). Two possible source mechanisms for the observed intrinsic planetary magnetic field are evaluated: an active dynamo and a passive paleomagnetic field frozen into the planet's outer layers at an earlier epoch. It is noted that neither the available magnetic-field data nor models of the planetary interior permit one to distinguish uniquely between the two mechanisms (Ness 1978). Different approximations of the main magnetic field by dipolar, quadrupolar and octupolar components were suggested based on these measurements (Ness 1979). The results of the Mariner 10 mission about the Hermean magnetic

field have not been fully explained in spite of many subsequent hypotheses (see, e.g., Strom and Sprague 2003 for their short description). Knowledge of the external magnetic field is the primary limiting factor in extracting reliable knowledge of the structure of Mercury's magnetic field from future observations (Korth et al. 2004).

Permanent magnetism and conventional dynamo theory are possible explanations for the magnitude of the Mercurian magnetic field, according to the point of view expressed by Stevenson (1987). A model was proposed and developed (Stevenson 1987; Schubert et al. 1988) in which thermoelectric currents driven by temperature differences at a bumpy core–mantle boundary are responsible for the (unobserved) toroidal field, and the helicity of convective motions in a thin outer core (thickness of about 100 km) induces the observed poloidal field from the toroidal field. The observed field of about 300 nT can be reproduced provided the electrical conductivity of Mercury's semiconducting mantle approaches 1,000/ohm per m. Tidal heating in the solid inner core plays the role of an additional heat source in this model. This model may be testable by future missions to Mercury. It predicts more complicated field geometry than conventional dynamo theories. However, it is argued that polar wander may cause the core–mantle topography to migrate so that some aspects of the rotational symmetry may be reflected in the observed field. Giampieri and Balogh (2002) reconsidered the thermoelectric dynamo model for the generation of the magnetic field of Mercury including its multipole expansion. Takahashi and Matsushima (2006) examined dynamo action possibly working in the fluid core of Mercury using numerical models in a thin spherical shell. Both dipolar and multipolar regimes are found for columnar flows inside and outside tangent cylinder. These results suggest that Mercury may have more complicated magnetic field than has been considered. Possibility was indicated of the robust testing of the further developed dynamo model by correlating future measurements of Mercury's magnetic and gravitational fields (Giampieri and Balogh 2002). Spohn and Breuer (2005), based on their calculations, found that the stagnant lid tends to thermally insulate the deep interior and fluid outer core shells for reasonable mantle rheology parameters even for compositions with as little as 0.1 weight% sulphur. The cooling time of the core can be much longer than naively assumed in the past. Radio measurements of the planetary rotation, using highly accurate radar speckle methods, are intended to find signatures of the existence of the molten interiors (Holin 1988; Van Hoolst et al. 2007). For an up-to-date review of the internal, dynamo-generated magnetic field of Mercury, see Wicht et al. (2007).

Stephenson (1976) suggested that the magnetic dipole moment of Mercury can be explained on the basis of thermoremanent magnetization acquired by an outer shell in an ancient Mercurian field produced by an internal dipole source such as a core dynamo which is now inactive. Such a shell will give rise to a dipole moment provided that there are differences of permeability between the shell and the interior, or the shell and free space. By assuming that the magnetic properties of the surface rocks of Mercury are similar to those of the moon it is shown that ancient fields of the order of 1 gauss and free iron concentrations of the order of a few percent are sufficient to produce the present dipole moment. We further develop this hypothesis and suggestion by Ksanfomality (1998a, 1998b, 2001) of possible similarity with the Moon and especially with Mars, where multiple crustal blocks exist with different remanent magnetization, but we do not exclude other hypotheses listed by Strom and Sprague (2003). In particular, liquid dynamo and solid magnets can coexist and contribute as in the case of Earth, but with different proportions between both contributors depending on specific evolutionary and structural details, which are not investigated now. Future measurements are needed to clarify the situation.

We have attempted to put some upper limits on the residual local magnetic fields, which could be tentatively associated with the local remanent magnetization of crustal blocks of Mercury's solid material based on available data.

## 11.2 Available Data and Method of Analysis

Available plots and numerical listings of 1.2-, 6-, and 42-s averages of magnetic field (Leping R.P., Ness N.F., and Behannon K.W., <http://nssdc.gsfc.nasa.gov/database/MasterCatalog?ds=PSFP-00072>) can be used to calculate residual magnetic fields  $B_{\text{residual}}$  which are defined as the difference between measured  $B_{\text{measured}}$  and modelled main magnetic field  $B_{\text{main}}$  vectors  $B_{\text{residual}} = B_{\text{measured}} - B_{\text{main}}$ . The value  $B_{\text{main}}$  represents here some model field. Estimates of residual magnetic fields were obtained by the visual inspection of corresponding plots. They are of the order of several nT (up to several tens of nT) depending on the approximation and model used for  $B_{\text{main}}$  (actually, dipole or dipole plus one-two further lowest harmonics). Residual magnetic fields can contain contributions from internal and external magnetic fields produced by planetary and heliospheric ‘sources of the magnetism’ (this terminology is not good, but still used: magnetic field is divergenceless and has no sources by its definition!) not considered in the main field model and also by possible errors of measurements. Let us assume experimental errors being negligible and consider plausible models of the residual field.

The magnetic field around Mercury is produced by the internal electric currents and magnetization of the body of the planet and by magnetospheric electric currents. Mercury’s internal magnetic fields are difficult to measure separately from magnetospheric contributions (see, e.g., Russell and Luhmann 1997). Magnetospheric currents strongly contribute to the measured field in the case, even at small orbital radii because of the small size of the magnetosphere. Giampieri et al. (2004) suggested exploiting the fact that the orbital and rotation periods of Mercury are nonsynchronous, in order to disentangle the internal field from external contributions. They simulated the magnetic field measurements onboard both BepiColombo orbiters (MMO and MPO) using for this purpose a Tsyganenko-type model for the Hermean magnetosphere, including contributions from the magnetopause and tail currents, as well as from reconnection. Using standard inversion techniques, these authors showed how to disentangle the magnetospheric field, periodically modulated by the orbital motion around the Sun, from the static internal field and concluded that collecting data from both orbiters over one or more orbital periods will give a good result. This procedure allows a fairly accurate measurement of the internal field multipoles, including higher order terms. Scuffham and Balogh (2006) developed a new empirical model of the Hermean field which is constrained wherever possible by the Mariner 10 data set. This model represents an appropriate rescaling of the Earth’s magnetic field model to the Hermean conditions and can be used to fit a much larger spacecraft data set when it becomes available.

## 11.3 On the Models and Estimates of the Residual Magnetic Field

Mapping Mercury’s internal magnetic field with a magnetometer in closed orbit around the planet will provide valuable information about its internal structure. By measuring magnetic field multipoles of order higher than the dipole one could, in principle, determine some properties, such as size and location, of the internal source. These expectations were quantified using conceptual models and simulation of actual measurement during the BepiColombo mission as well as analyzing the simulated data in order to estimate the measurement errors due to the limited spatial sampling. Ability to locate the field-generating current system within the planet and main limitation of the model, due to the presence of time-varying external magnetospheric currents was investigated (Giampieri and Balogh 2001). Our model assumptions differ from that of the paper by Giampieri and Balogh (2001) in several respects. In particular, we do not assume a priori an axial symmetry. We consider the residual field, tentatively, to consist of several or many blocks similar to magnetized strips and

anomalies possibly associated with traces of ancient eruptions, impacts and dynamo action on Mars.

Balogh and Giampieri (2002) pointed out that it is unlikely that the Hermean magnetic field is dominated by the dipolar term; multipolar terms (quadrupole, octupole and higher order terms) are probably more important, when compared to the dipole, than in the case of the Earth. The main reason for this is that the location of the generation mechanism, at the vicinity of the core–mantle boundary, is much closer to the surface of the planet, due to the large size of the core, than at the Earth. Whether the field is generated by a hydrodynamic dynamo in a molten outer layer of the core, or by a thermoelectric dynamo at the core–mantle boundary, the mechanisms yield relatively significant higher order multipolar terms. Grosser et al. (2004), based on their two-layer model of Mercury on calculated contributions of magnetospheric or induced currents, depending on the core size.

The crustal magnetization can be observable or hidden depending on its strength and orientation. The horizontally oriented elementary magnets organized in linear or surface structures can be practically ‘invisible’ under appropriate geometry conditions. Only diffusion fields at the ends of such structures appear and can be measured above the surface of the planet. Vertically oriented magnetization is more easily observable from space because of the magnetic flux conservation and field line divergence from stronger fields to weaker ones. Divergence of the field lines with the altitude from ‘local poles’ at such places is smallest or could be even negligible in the case of large magnetized areas, when their linear size is larger than the altitude of the observation point. For the vertically placed thin sheet with the vertical magnetization along them one obtains rather slow decrease of the field with altitude above the edge. For linear structures which are thin in comparison with the altitude of observation and placed horizontally one obtains a two-dimensional situation with faster decrease of magnetic field strength as a function of the altitude. An even faster decrease follows for point-like ‘poles’. Elementary considerations described in textbooks (Stratton 1941; Smythe 1950) give well-known results for different geometry.

The inverse mathematical problem that consists of determining unknown ‘sources’ (electric currents, magnetization fields near and beneath the surface) when the fields are given at one level above the surface is usually ill posed and has no unique solution when additional information is not known. This additional information is used practically for the reformulation of the inverse problem and to its ‘regularization’, i.e., to finally have well-determined solvable problems with unique and stable solutions. Corresponding numerical procedures are especially developed in the geophysics (Zhdanov 2002).

It is not useful to discuss and construct different quantitative, plausible and simplistic models at this stage, because of our limited input information about approximations for their selection. It is enough for our purposes to limit consideration by simple and very rough order of magnitude estimates taking into account a broad range of possible real situations behind scarce observations.

Based on these arguments, we performed the visual and qualitative inspection of data and models. The smooth dome-like shape of the magnetic field plot (Ness et al., 1975a, 1975b) obtained during the close approach (flyby III) with no large deviations from the main field indicates the absence of strong anomalies in the vertical magnetization on the ground beneath the spacecraft. As was also mentioned earlier, based on expert estimates of these residuals we obtained in this way upper limits between several nT and several tens of nT for the residual vertical fields on the ground, averaged over distances of several hundred km along the path of the Mariner 10 during its third flyby. We interpret this result as an indication of small anomalies, if any at the mentioned level of accuracy, in investigated regions

around two lines—projections of the flyby trajectories on the surface of the planet. The interpretation is heavily dependent on the hypothesis that the main field can be considered separately and it is not of crustal origin.

#### 11.4 On Possible Origins of Crustal Fields on Mercury

We propose that crustal magnetic fields on Mercury appeared after cooling of the magnetized fluid fraction below the Curie temperature. The magnetization of the fluid could be produced by electric currents (so-called MHD dynamo action). Some specific conditions are needed for the magnetic field self-generation, which can be fulfilled or not under given physical conditions and prehistory. Prehistory and ‘memory’ play a role in the nonlocal problem with many essential time scales for evolution and dissipation. There is no reliable scenario of the past MHD dynamo in Mercury at the moment and we can only speculate on its presence and characteristics.

We can suggest a possible scenario of the crustal magnetization process based on the available fragmentary information described above. The first step is the collision between comparable planetary bodies (formation of the Basin S could be the marker of the date and the size of this event). The relative velocity of the colliding bodies should be intermediate—not too large and not too small. For rather large relative velocities of colliding bodies (of the order of 10 km/s) their catastrophic destruction and subsequent disappearance of fragments and evaporation should be a consequence. For small relative velocities a slow, non-catastrophic gravitational merging process is not excluded. Such a process could lead to the formation of a jointed and rather cool solid body with no melting. At the intermediate relative velocities, an intermediate situation is conceivable: inelastic collision with the partial loss of mass in the shape fragments and partial melting and evaporation. Large, intermediate and small velocities are scaled by the characteristic thermal and gravitational escape velocities. The newly formed main body could be larger or smaller than initial colliding bodies. It could be solid, partially or completely melted depending on many unknown details of process. The proportion between different phases (solid, liquid, vapours, etc.) and fragments is difficult to estimate—it depends on many unknown details (composition, structure, velocity etc.).

We assume that the fluid fraction on Mercury was formed because of melting after its parent body collision with another celestial body of lesser, but comparable mass. We do not know when this hypothetical event happened—more studies are needed to clarify the age. A partial loss could happen of joint mass and partial melting of a newly formed jointed body. The hypothesis about a large collision is not new (see, e.g., Hartmann 1983). We find an indication of this event in the past: recent observations probably show huge (1,000–2,000 km) concentric structures on Mercury at longitudes 260–285°W (Ksanfomality 1998a, 1998b; Ksanfomality et al. 2005). These observations have been apparently confirmed by other methods (see, Harmon 2007, for the description of the radiolocation data and results, which initially did not show a clear confirmation). It is not excluded that Mercury, in the past, inelastically collided with another celestial body. We assume that the collision happened indeed and was not completely catastrophic for Mercury, which survived. The resulting mass of the newly formed main body (presumably present Mercury) after the collision can be larger or less than the mass of each initial colliding counterpart. There are also geological hints that the outer layers of mass were lost due to collisional sputtering of fragments and the remaining ‘iron Mercury’ was formed in this way.

We assume in our tentative scenario comparable masses of colliding bodies and anticipate the situation of an inelastic collision with appreciable melting of a large part of the newly

formed planetary body. If masses are significantly different, the resulting mass of liquid is obviously not so large. Hence, we assume intermediate velocities, presumably, of the order of hundreds of meters per second or roughly, 1 km/s. Most elaborated numerical runs in the case of Mercury were performed only for higher relative velocities of about 20–30 km/s or so (Benz et al. 1988; Benz 2007). If the newly formed planet is partially or completely liquid, then standard dynamo action would work and produce magnetic fields. Subsequent cooling below the Curie point will produce crystal magnetization of solidified blocks, which is preserved up to present times and observed. Partial demagnetization of the crust can also occur due to heating by subsequent collisions with numerous smaller bodies (Artemieva et al. 2005), but these processes were not evaluated in the case of Mercury.

If our hypothesis is correct and the elapsed time is not enough to ‘forget’ about this collision and smear-out the memory of its consequences, we expect a rather strong internal asymmetry preserved inside the planet. A noncentred magnetic dipole and higher harmonics could be the natural manifestations of this memory. An actual dynamo can operate now or not; it is an open issue to be tested only in very long-term observations. Instantaneous measurements or short time episodes are not sufficient for any reliable conclusions. The measurements of the dynamical geology and dynamical magnetic fields are necessary for the separation of possible solid body and fluid contributions. The situation is similar in the geomagnetism. This point was correctly stressed by Connerney and Ness (1988).

The acquisition of thermoremanent magnetization (TRM) by a cooling spherical shell was studied for internal magnetizing dipole fields, using Runcorn’s (1975b) theorems on magnetostatics (Srňka 1976). If the shell cools progressively inward, inner regions acquire TRM in a net field composed of the dipole source term plus a uniform field due to the outer magnetized layers. In this case, the global dipole moment and external remanent field are nonzero when the whole shell has cooled below the Curie point and the source dipole has disappeared. The remanent field outside the shell is found to depend on the thickness, radii, and cooling rate of the shell, as well as the coefficient of TRM and the intensity of the magnetizing field (Srňka 1976). In reality, Runcorn’s theorems are not so essential and do not restrict the magnetization in the absence of spherical symmetry. We assume this situation.

The measured ‘pole/equator ratio’ for magnetic field on Mercury, i.e., the ratio of Mercury III to Mercury I maximal fields is rather large, about 3. It is larger than for the corresponding ‘pole/equator ratio’ in the case of the central dipole. This last value is equal to 2. Higher multipoles (quadrupole, octupole, etc.), large external magnetospheric fields (tail currents, Chapman–Ferraro currents, Birkeland currents, substorm currents, etc.) have been invoked as a possible explanation. We should remark that Fig. 5 in the paper by Ksanfomality (1998b) can be also interpreted as an indication of the possible strip magnetization of Mercury. Three to five strips extended along the meridian direction with a similar magnetization along them (or six to ten strips with opposite magnetization plus general field of larger scale) could provide the observed magnetic pattern for these two passes. In this case, the global dipole would be formed from the bundle of magnetic tubes or sheets presumably oriented close to the axis of the planet and placed at longitudes associated in some way with S Basin position at present time. The remaining magnetic field could be formed by the dispersion fields of finite length magnetic tubes and other sources. (In the case of Mars, this orientation of magnetic ribbons is along the parallels in the southern hemisphere.)

Ksanfomality (1998b) assumed two to three differently oriented blocks (500–1,000 km each in size) not specifying the shape and intensity. We speculate further about their elongated shape and field intensity, which depends on details of geometry and placement: tens to hundreds Gauss in the tubes for their compact position near the centre of the planet (this

variant is not favourable for the explanation of the data) or more moderate and lower values up to hundreds of nanoTesla with different, ‘more realistic’ assumptions about the geometry and placement closer to the surface. The term ‘realistic’ is not quite correct in this context noting the lack of sufficient data to resolve the ambiguity and can be understood in the sense of a higher likelihood only.

The hypotheses of the combined (crustal and transient substorm-like) origin of the magnetic peculiarities is not excluded at the present scarce level of our knowledge after Mariner 10 about the Hermean magnetic field structure and its time variations, but this question needs further investigation. We can also speculate further that the situation can be partially similar in this respect to the Martian and terrestrial ones with their active magnetospheres, but not to the lunar case. Martian magnetic fields have relic crustal origins, nevertheless many important questions remain open (Acuna et al. 1999; Connerney et al., 2001, 2004a, 2004b; Kletetschka et al. 2005; Langlais et al. 2004). Lunar magnetic fields also have unclear origins (Runcorn 1975a, 1975b; Dolginov 1993; Richmond et al. 2003). The comparative study can bring new valuable constraints on the cosmogenic scenarios, which are far from being completed now.

## References

- M.H. Acuna, J.E.P. Connerney, N.F. Ness, R.P. Lin, D. Mitchell, C.W. Carlson, J. McFadden, K.A. Anderson, H. Reme, C. Mazelle, D. Vignes, P. Wasilewski, P. Cloutier, Global distribution of crustal magnetization discovered by the Mars global surveyor MAG/ER experiment. *Science* **284**(5415), 790 (1999)
- L.A. Akimov, On the brightness distribution across the lunar disk and planets. *Astron. Zh.* **56**, 412–418 (1979) (in Russian)
- L.A. Akimov, Reflection of light by the Moon I. *Kinematika Fiz. Nebesnikh Tel.* **4**(1), 3–10 (1988) (in Russian)
- L.A. Akimov, Y.V. Kornienko, Light scattering by the lunar surface. *Kinematika Fiz. Nebesnikh Tel.* **10**(2), 15–22 (1994) (in Russian)
- N. Artemieva, L. Hood, B.A. Ivanov, Impact demagnetization of the Martian crust: Primaries versus secondaries. *Geophys. Res. Lett.* **32**(22) (2005). doi:[10.1029/2005GL024385](https://doi.org/10.1029/2005GL024385)
- A. Balogh, G. Giampieri, The origin of Mercury’s magnetic field and its multipolar structure. EGS XXVII General Assembly, Nice, 21–26 April 2002, abstract #5959
- J. Baumgardner, M. Mendillo, J.K. Wilson, Digital high-definition imaging system for spectral studies of extended planetary atmospheres. 1. Initial results in white light showing features on the hemisphere of Mercury unimaged by Mariner 10. *Astron. J.* **119**, 2458–2464 (2000)
- W. Benz, *Space Sci. Rev.* (2007, this issue)
- W. Benz, W.L. Slattery, A.G.W. Cameron, Collisional stripping of Mercury’s mantle. *Icarus* **74**, 516–528 (1988)
- B.J. Buratti, J. Veverka, Voyager photometry of Europa. *Icarus* **55**, 93–110 (1983)
- B.J. Butler, D.O. Muhleman, M.A. Slade, Mercury – Full-disk radar images and the detection and stability of ice at the North Pole. *J. Geophys. Res.* **98**, 15003–15023 (1993)
- S. Chandrasekhar, *Radiative Transfer* (Dover, New York, 1960)
- S.C. Chase, E.D. Miner, D. Morrison et al., Preliminary infrared radiometry of the night side of Mercury from Mariner 10. *Science* **185**, 142–145 (1974)
- J.E.P. Connerney, N.F. Ness, Mercury’s magnetic field and interior, in *Mercury* (University of Arizona Press, Tucson, 1988), pp. 494–513
- J.E.P. Connerney, M.H. Acuña, P.J. Wasilewski, G. Kletetschka, N.F. Ness, H. Rème, R.P. Lin, D.L. Mitchell, The global magnetic field of Mars and implications for crustal evolution. *Geophys. Res. Lett.* **28**(21), 4015–4018 (2001). doi:[10.1029/2001GL013619](https://doi.org/10.1029/2001GL013619)
- J.E.P. Connerney, M.H. Acuña, N.F. Ness, T. Spohn, G. Schubert, Mars crustal magnetism. *Space Sci. Rev.* **111**(1), 1–32 (2004a)
- J.E.P. Connerney, M.H. Acuna, N.F. Ness, D.L. Mitchell, R.P. Lin, H. Reme, A magnetic perspective on the Martian crustal dichotomy. Hemispheres Apart: the Origin and Modification of the Martian Crustal Dichotomy. LPI Contribution No. 1213. Proceedings of the conference held September 30–October 1, 2004, in Houston, TX, USA, 2004b, pp. 11–12

- A.C. Cook, M.S. Robinson, Mariner 10 stereo image coverage of Mercury. *J. Geophys. Res.* **105**(E4), 9429–9443 (2000)
- A. Danjon, Photometrie et colorimetrie des planetes Mercure et Venus. *Bull. Astron.* **14**, 315 (1949)
- R.F. Dantowitz, S.W. Teare, M.J. Kozubal, Ground based-based high-resolution imaging of Mercury. *Astron. J.* **119**, 2455–2457 (2000)
- M.E. Davies, S.E. Dwornik, D.E. Gault, R.G. Strom, Atlas of Mercury, in *NASA Scientific and Technical Report*, ed. by J. Dunn, NASA SP-42 (US Government Printing Office, Washington, 1978)
- A.Z. Dolginov, Magnetic fields and nonuniform structures of the Moon. Twenty-fourth Lunar and Planetary Science Conference. Part 1: A-F, 1993, pp. 411–412
- A. Dollfus, Pic-du-Midi visual and photographic observations of planets, in *Planets and Satellites*, ed. by G.P. Kuiper, B.M. Middlehurst (The University of Chicago Press, Chicago, 1961), pp. 482–485
- A. Dollfus, M. Auriere, Optical polarimetry of planet Mercury. *Icarus* **23**, 465 (1974)
- D. Domingue, B. Hapke, Fitting theoretical photometric functions to asteroid phase curves. The scattering properties of natural terrestrial snows versus icy satellite surfaces. *Icarus* **78**, 330–336 (1989)
- D. Domingue, B. Hartman, A. Verbiscer, The scattering properties of natural terrestrial snows versus icy satellite surfaces. *Icarus* **128**, 28–48 (1997)
- J.P. Emery, A.L. Sprague, F.C. Witteborn, J.E. Colwell, D.H. Kozlowski, R.W.H. Wooden, Mercury: Thermal modeling and mid-infrared (5–12  $\mu\text{m}$ ) observations. *Icarus* **136**, 104 (1998)
- D.L. Fried, Probability of getting a lucky short-exposure image through turbulence. *J. Opt. Soc. Am.* **68**, 1651–1658 (1978)
- P.E. Geissler, A. McEwen, L. Keszthelyi, R. Lopes-Gautier, J. Granahan, D.P. Simonelli, Global color variations on Io. *Icarus* **140**, 265–282 (1999)
- G. Giampieri, A. Balogh, Modelling of magnetic field measurements at Mercury. *Planet. Space Sci.* **49**(14–15), 1637–1642 (2001)
- G. Giampieri, A. Balogh, Mercury's thermoelectric dynamo model revisited. *Planet. Space Sci.* **50**(7–8), 757–762 (2002)
- G. Giampieri, J. Scuffham, A. Balogh, BepiColombo measurements of Mercury's internal field. 35th COSPAR Scientific Assembly. Held 18–25 July 2004, in Paris, France, 2004, p. 2726
- J. Gradie, J. Veverka, Photometric properties of powdered sulfur. *Icarus* **58**, 227–245 (1984)
- J. Grosser, K.-H. Glassmeier, A. Stadelmann, Magnetic field effects at planet Mercury. *Planet. Space Sci.* **52**(14), 1251–1260 (2004)
- E.W. Guinness, R.E. Arvidson, I. Clark, M.K. Shepard, Optical scattering properties of terrestrial varnished basalts compared with rocks and soils at the Viking Lander sites. *J. Geophys. Res.* **102**, 28687–28703 (1997)
- K. Gunderson, J.A. Whitby, N. Thomas, Visible and NIR BRDF Measurements of Lunar Soil Simulant, 36th Annual Lunar and Planetary Science Conference, abstract no. 1781, 2005
- K. Gunderson, N. Thomas, J.A. Whitby, First measurements with the Physikalisches Institut Radiometric Experiment (PHIRE). *Planet. Space Sci.* **54**(11), 1046–1056 (2006)
- B. Hapke, Bidirectional reflectance spectroscopy. 1. Theory. *J. Geophys. Res.* **86**, 3039–3054 (1981)
- B. Hapke, Bidirectional reflectance spectroscopy. 3. Correction for macroscopic roughness. *Icarus* **59**, 41–59 (1984)
- B. Hapke, Bidirectional reflectance spectroscopy. 4. The extinction coefficient and the opposition effect. *Icarus* **67**, 264–280 (1986)
- B. Hapke, *Theory of Reflectance and Emittance Spectroscopy* (Cambridge Univ. Press, New York, 1993)
- B. Hapke, Bidirectional reflectance spectroscopy. 5. The coherent backscatter opposition effect and anisotropic scattering. *Icarus* **157**, 523–534 (2002)
- J.K. Harmon, *Space Sci. Rev.* (2007, this issue). doi:[10.1007/s11214-007-9234-y](https://doi.org/10.1007/s11214-007-9234-y)
- J.K. Harmon, D.B. Campbell, Radar observations of Mercury, in *Mercury*, ed. by F. Vilas, C.R. Chapman, M.S. Matthews (Univ. of Arizona, Tucson, 1988), pp. 101–117
- J.K. Harmon, M.A. Slade, Radar mapping of Mercury: Full-disk images and polar anomalies. *Science* **258**, 640–642 (1992)
- J.K. Harmon, P.J. Perillat, M.A. Slade, High-resolution radar imaging of Mercury's North Pole. *Icarus* **149**, 1–15 (2001)
- J.K. Harmon, M.A. Slade, B.J. Butler, J.W. Head, M.S. Rice, D.B. Campbell, Mercury: Radar images of the equatorial and mid-latitude zones. *Icarus* **187**, 374 (2007)
- W.K. Hartmann, *Moons and Planets* (Wadsworth Publishing Co., Belmont, 1983), Chap. 5, 510 p
- J.W. Head, III, Surfaces of the terrestrial planets, in *The New Solar System*, ed. by J.K. Beatty et al. (Sky Publishing Corporation, London, 1981), pp. 45–56
- I.V. Holin, Space-time coherence of signal scattered by diffuse moving surface in case of arbitrary motion and monochromatic illumination. *Radiophys. Quantum Electron.* **31**, 515–518 (1988) (in Russian)

- P. Helfenstein, J. Veverka, Photometric properties of lunar terrains derived from Hapke's equation. *Icarus* **72**, 342–357 (1987)
- J.K. Hillier, J. Veverka, P. Helfenstein, P. Lee, Photometric diversity of terrains on Triton. *Icarus* **109**, 296–312 (1994)
- R.E. Hufnagel, Restoration of atmospherically degraded images. *Proc. Nat. Acad. Sci.* **3**, App. 2, 11 (1966)
- J.R. Johnson, W.M. Grundy, M.T. Lemmon, J.F. Bell III, M.J. Johnson, R. Deen, R.E. Arvidson, W.H. Farrand, E. Guinness, A.G. Hayes, K.E. Herkenhoff, F. Seelos IV, J. Soderblom, S. Squyres, Spectrophotometric properties of materials observed by Pancam on the Mars Exploration Rovers. 1. Spirit. *J. Geophys. Res.* **111**(E02S14) (2006). doi:[10.1029/2005JE002494](https://doi.org/10.1029/2005JE002494)
- V.O. Kakhiani, Astronomical image processor AIMAP (2003, unpublished)
- G. Kletetschka, N.F. Ness, J.E.P. Connerney, M.H. Acuna, P.J. Wasilewski, Grain size dependent potential for self-generation of magnetic anomalies on Mars via thermoremanent magnetic acquisition and magnetic interaction of hematite and magnetite. *Phys. Earth Planet. Interiors* **148**(2–4), 149–156 (2005)
- H. Korth, J.B. Anderson, M.H. Acuna, J.A. Slavin, N.A. Tsyganenko, S.C. Solomon, R.L. McNutt, Determination of the properties of Mercury's magnetic field by the MESSENGER mission. *Planet. Space Sci.* **52**(8), 733–746 (2004)
- M.A. Kreslavsky, Y.G. Shkuratov, Y.I. Velikodsky, V.G. Kaydash, D.G. Stankevich, Photometric properties of the lunar surface derived from Clementine observations. *J. Geophys. Res.* **105**(E8), 20281–20295 (2000)
- L.V. Ksanfomality, Proper magnetic fields of planets and satellites (a review). *Sol. Syst. Res.* **32**(1), 31–41 (1998a)
- L.V. Ksanfomality, The magnetic field of Mercury: A revision of the Mariner 10 results. *Sol. Syst. Res.* **32**(2), 115–121 (1998b)
- L.V. Ksanfomality, Physical properties of the Hermean surface (a review). *Sol. Syst. Res.* **35**(5), 339–353 (2001)
- L.V. Ksanfomality, High-resolution imaging of Mercury using Earth-based facilities. *Sol. Syst. Res.* **36**, 267–277 (2002)
- L.V. Ksanfomality, Mercury: Image of the planet in the longitude interval 210–285°W obtained by method of short exposures. *Sol. Syst. Res.* **37**, 514–525 (2003)
- L.V. Ksanfomality, A huge basin in the unknown portion of Mercury in the 250–290°W longitude range. *Sol. Syst. Res.* **38**, 21–27 (2004)
- L.V. Ksanfomality, Global asymmetry of large forms of Hermean relief. The 2nd AOGS session, 2005, June, Singapore, Paper ID: 58-PS-A0974, 2005
- L.V. Ksanfomality, Earth-based optical imaging of Mercury. *Adv. Space Res.* **38**, 594–598 (2006)
- L. Ksanfomality, A.L. Sprague, New images of Mercury's surface from 210° to 290°W longitudes with implications for Mercury's global asymmetry. *Icarus* (2007). doi:[10.1016/j.icarus.2006.12.009](https://doi.org/10.1016/j.icarus.2006.12.009)
- L.V. Ksanfomality, V.P. Dzhapiashvili, V.O. Kakhiani, A.K. Mayer, Experiment on obtaining of Mercury's images by the short exposure method. *Sol. Syst. Res.* **35**, 190–194 (2001)
- L. Ksanfomality, G. Papamastorakis, N. Thomas, The planet Mercury: Synthesis of resolved images of unknown part in the longitude range 250–290°W. *Planet. Space Sci.* **53**, 849–859 (2005)
- J.H. Lambert, *Photometria Sive de Mensura et Gradibus Luminis, Colorum et Umbrae*. Detleffsen, Augsburg, 1760
- B. Langlais, M.E. Purucker, M. Mandea, Crustal magnetic field of Mars. *J. Geophys. Res.* **109**(E2) (2004). doi:[10.1029/2003JE002048](https://doi.org/10.1029/2003JE002048)
- P.G. Lucey, D.T. Blewett, B.L. Joliff, Lunar iron and titanium abundance algorithms based on final processing of Clementine ultraviolet-visible images. *J. Geophys. Res.* **105**(20), 297 (2000a)
- P.G. Lucey, D.T. Blewett, G.J. Taylor, B.R. Hapke, Imaging of lunar surface maturity. *J. Geophys. Res.* **105**(20), 377 (2000b)
- A. Mallama, D. Wang, R.A. Howard, Photometry of Mercury from SOHO/LASCO and Earth. The Phase Function from 2 to 170 deg. *Icarus* **155**, 253 (2002)
- Red Shift 4. Maris Multimedia Ltd, 2000. [www.cinegram.com](http://www.cinegram.com)
- A.S. McEwen, Photometric functions for photoclinometry and other applications. *Icarus* **92**, 298–311 (1991)
- M. Mendillo, J. Warell, S.S. Limaye, J. Baumgardner, A. Sprague, J.K. Wilson, Imaging the surface of Mercury using ground-based telescopes. *Planet. Space Sci.* **49**, 1501 (2001)
- M. Minnaert, The reciprocity principle in lunar photometry. *Astrophys. J.* **93**, 403–410 (1941)
- D.L. Mitchell, I. de Pater, Microwave imaging of Mercury's thermal emission at wavelengths from 0.3 to 20.5 cm. *Icarus* **110**, 2 (1994)
- J. Murray, A. Dollfus, B. Smith, Cartography of the surface markings of Mercury. *Icarus* **17**, 576–584 (1972)
- N.F. Ness, Mercury—Magnetic field and interior. *Space Sci. Rev.* **21**, 527–553 (1978)
- N.F. Ness, The magnetic field of Mercury. *Phys. Earth Planet. Interiors* **20**, 209–217 (1979)

- N.F. Ness, K.W. Behannon, R.P. Lepping, Y.C. Whang, Magnetic field of Mercury confirmed. *Nature* **255**, 204–205 (1975a)
- N.F. Ness, K.W. Behannon, R.P. Lepping, Y.C. Whang, The magnetic field of Mercury. I. *J. Geophys. Res.* **80**, 2708–2716 (1975b)
- N.F. Ness, K.W. Behannon, R.P. Lepping, Y.C. Whang, Observations of Mercury's magnetic field. *Icarus* **28**, 479–488 (1976)
- R.T. Pappalardo, J.W. Head, G.C. Collins, R.L. Kirk, G. Neukum, J. Oberst, B. Giese, R. Greeley, C.R. Chapman, P. Helfenstein, J.M. Moore, A. McEwen, B.R. Tufts, D.A. Senske, H.H. Breneman, K. Klaasen, Grooved terrain on Ganymede: First results from Galileo highresolution imaging. *Icarus* **135**, 276–302 (1998)
- N.C. Richmond, L.L. Hood, J.S. Halekas, D.L. Mitchell, R.P. Lin, M. Acuña, A.B. Binder, Correlation of a strong lunar magnetic anomaly with a high-albedo region of the Descartes mountains. *Geophys. Res. Lett.* **30**(7), 48–51 (2003). doi:[10.1029/2003GLO16938](https://doi.org/10.1029/2003GLO16938)
- S.K. Runcorn, An ancient lunar magnetic dipole field. *Nature* **253**, 701–703 (1975a)
- S.K. Runcorn, On the interpretation of lunar magnetism. *Phys. Earth Planet. Interiors* **10**(4), 327–335 (1975b)
- C.T. Russell, J.G. Luhmann, Mercury: Magnetic field and magnetosphere, in *Encyclopedia of Planetary Sciences*, ed. by J.H. Shirley, R.W. Fairbridge (Chapman & Hall, London, 1997), pp. 476–478
- G. Schubert, M.N. Ross, D.J. Stevenson, T. Spohn, Mercury's thermal history and the generation of its magnetic field Mercury, in *Mercury* (University of Arizona Press, Tucson, 1988), pp. 429–460
- J. Scuffham, A. Balogh, A new model of Mercury's magnetospheric magnetic field. *Adv. Space Res.* **38**, 616–626 (2006)
- M.A. Slade, B.J. Butler, D.O. Muhleman, Mercury radar imaging—Evidence for polar ice. *Science* **258**, 635 (1992)
- W.R. Smythe, *Static and Dynamic Electricity* (McGraw-Hill, 1950)
- T. Spohn, D. Breuer, Core composition and the magnetic field of Mercury, American Geophysical Union, Spring Meeting 2005, abstract #P23A-01
- A.L. Sprague, R.W.H. Kozlowski, D.M. Hunten, Caloris Basin: An enhanced source for potassium in Mercury's atmosphere. *Science* **249**, 1140–1143 (1990)
- A.L. Sprague, L.K. Deutsch, J. Hora, G.G. Fazio, B. Ludwig, J. Emery, W.F. Hoffmann, Mid-infrared (8.1–12.5  $\mu\text{m}$ ) imaging of Mercury. *Icarus* **147**, 421 (2000)
- A.L. Sprague, J.P. Emery, K.L. Donaldson, R.W. Russell, D.K. Lynch, A.L. Mazuk, Mercury: Mid-infrared (3–13.5  $\mu\text{m}$ ) observations show heterogeneous composition, presence of intermediate and basic soil types, and pyroxene. *Meteorit. Planet. Sci.* **37**, 1255 (2002)
- A.L. Sprague, J. Warell, J. Emery, A. Long, R.W.H. Kozlowski, Mercury: First spectra from 0.7 to 5.5  $\mu\text{m}$  support low FeO and feldspathic composition. 35th Lunar and Planetary Science Conference, 2004, abstract no. 1630
- S.W. Squyres, J. Veverka, Voyager photometry of surface features on Ganymede and Callisto. *Icarus* **46**, 137–155 (1981)
- L.J. Srnka, Magnetic dipole moment of a spherical shell with TRM acquired in a field of internal origin. *Phys. Earth Planet. Interiors* **11**(3), 184–190 (1976)
- R. Stekelenburg, AstroStack manual (v. 0.90 beta), 1999, 2000. <http://www.astrystack.com/>
- A. Stephenson, Crustal remanence and the magnetic moment of Mercury. *Earth Planet. Sci. Lett.* **28**(3), 454–458 (1976)
- D.J. Stevenson, Mercury's magnetic field—A thermoelectric dynamo? *Earth Planet. Sci. Lett.* **82**(1–2), 114–120 (1987)
- J.A. Stratton, *Electromagnetic Theory* (McGraw-Hill, 1941)
- R.G. Strom, A.L. Sprague, *Exploring Mercury: The Iron Planet* (Springer, Chichester, 2003), 216 pp
- F. Takahashi, M. Matsushima, Dipolar and non-dipolar dynamos in a thin shell geometry with implications for the magnetic field of Mercury. *Geophys. Res. Lett.* **33**(10) (2006), CiteID L10202
- T. Van Hoolst et al., *Space Sci. Rev.* (2007, this issue). doi:[10.1007/s11214-007-9202-6](https://doi.org/10.1007/s11214-007-9202-6)
- J. Veverka, P. Helfenstein, B. Hapke, J. Goguen, Photometry and polarimetry of Mercury, in *Mercury*, ed. by F. Vilas, C. Chapman, M. Matthews (Univ. of Arizona Press, Tucson, 1988), pp. 37–58
- F. Vilas, P.S. Cobian, N.G. Barlow, S.M. Lederer, How much material do the radar-bright craters at the mercurian poles contain? *Planet. Space Sci.* **53**, 1496–1500 (2005)
- J. Warell, Properties of the Hermean regolith: II. Disk-resolved multicolor photometry and color variations of the “unknown” hemisphere. *Icarus* **156**, 303 (2002)
- J. Warell, Properties of the Hermean regolith: III. Disk-resolved vis–NIR reflectance spectra and implications for the abundance of iron. *Icarus* **161**, 199–222 (2003)
- J. Warell, Properties of the Hermean regolith: IV. Photometric parameters of Mercury and the Moon contrasted with Hapke modelling. *Icarus* **167**, 271 (2004)

- J. Warell, D.T. Blewett, Properties of the Hermean regolith: V. New optical reflectance spectra, comparison with lunar anorthosites, and mineralogical modelling. *Icarus* **168**, 257 (2004)
- J. Warell, S.S. Limaye, Properties of the Hermean regolith: I. Global regolith albedo variation at 200 km scale from multicolor CCD imaging. *Planet. Space Sci.* **49**, 1531 (2001)
- J. Warell, P.-G. Vaegård, Albedo–color distribution on Mercury: A study of the poorly known hemisphere. *Astron. Astrophys.* **460**, 625 (2006)
- J. Wicht et al., *Space Sci. Rev.* (2007, this issue). doi:[10.1007/s11214-007-9280-5](https://doi.org/10.1007/s11214-007-9280-5)
- M.S. Zhdanov, *Geophysical Inverse Theory and Regularization Problems* (Elsevier, 2002)